GEOPHYSICAL MONOGRAPH SERIES

AGU
ADVANCING EARTH AND SPACE SCIENCES

Fast Processes in Large-Scale Atmospheric Models

Progress, Challenges, and Opportunities

Editors

Yangang Liu

Pavlos Kollias

WILEY

Fast Processes in Large-Scale Atmospheric Models

Geophysical Monograph Series

231 **Bioenergy and Land Use Change** *Zhangcai Qin, Umakant Mishra, and Astley Hastings (Eds.)*
232 **Microstructural Geochronology: Planetary Records Down to Atom Scale** *Desmond Moser, Fernando Corfu, James Darling, Steven Reddy, and Kimberly Tait (Eds.)*
233 **Global Flood Hazard: Applications in Modeling, Mapping, and Forecasting** *Guy Schumann, Paul D. Bates, Giuseppe T. Aronica, and Heiko Apel (Eds.)*
234 **Pre-Earthquake Processes: A Multidisciplinary Approach to Earthquake Prediction Studies** *Dimitar Ouzounov, Sergey Pulinets, Katsumi Hattori, and Patrick Taylor (Eds.)*
235 **Electric Currents in Geospace and Beyond** *Andreas Keiling, Octav Marghitu, and Michael Wheatland (Eds.)*
236 **Quantifying Uncertainty in Subsurface Systems** *Celine Scheidt, Lewis Li, and Jef Caers (Eds.)*
237 **Petroleum Engineering** *Moshood Sanni (Ed.)*
238 **Geological Carbon Storage: Subsurface Seals and Caprock Integrity** *Stephanie Vialle, Jonathan Ajo-Franklin, and J. William Carey (Eds.)*
239 **Lithospheric Discontinuities** *Huaiyu Yuan and Barbara Romanowicz (Eds.)*
240 **Chemostratigraphy Across Major Chronological Eras** *Alcides N. Sial, Claudio Gaucher, Muthuvairavasamy Ramkumar, and Valderez Pinto Ferreira (Eds.)*
241 **Mathematical Geoenergy: Discovery, Depletion, and Renewal** *Paul Pukite, Dennis Coyne, and Daniel Challou (Eds.)*
242 **Ore Deposits: Origin, Exploration, and Exploitation** *Sophie Decree and Laurence Robb (Eds.)*
243 **Kuroshio Current: Physical, Biogeochemical, and Ecosystem Dynamics** *Takeyoshi Nagai, Hiroaki Saito, Koji Suzuki, and Motomitsu Takahashi (Eds.)*
244 **Geomagnetically Induced Currents from the Sun to the Power Grid** *Jennifer L. Gannon, Andrei Swidinsky, and Zhonghua Xu (Eds.)*
245 **Shale: Subsurface Science and Engineering** *Thomas Dewers, Jason Heath, and Marcelo Sánchez (Eds.)*
246 **Submarine Landslides: Subaqueous Mass Transport Deposits From Outcrops to Seismic Profiles** *Kei Ogata, Andrea Festa, and Gian Andrea Pini (Eds.)*
247 **Iceland: Tectonics, Volcanics, and Glacial Features** *Tamie J. Jovanelly*
248 **Dayside Magnetosphere Interactions** *Qiugang Zong, Philippe Escoubet, David Sibeck, Guan Le, and Hui Zhang (Eds.)*
249 **Carbon in Earth's Interior** *Craig E. Manning, Jung-Fu Lin, and Wendy L. Mao (Eds.)*
250 **Nitrogen Overload: Environmental Degradation, Ramifications, and Economic Costs** *Brian G. Katz*
251 **Biogeochemical Cycles: Ecological Drivers and Environmental Impact** *Katerina Dontsova, Zsuzsanna Balogh-Brunstad, and Gaël Le Roux (Eds.)*
252 **Seismoelectric Exploration: Theory, Experiments, and Applications** *Niels Grobbe, André Revil, Zhenya Zhu, and Evert Slob (Eds.)*
253 **El Niño Southern Oscillation in a Changing Climate** *Michael J. McPhaden, Agus Santoso, and Wenju Cai (Eds.)*
254 **Dynamic Magma Evolution** *Francesco Vetere (Ed.)*
255 **Large Igneous Provinces: A Driver of Global Environmental and Biotic Changes** *Richard. E. Ernst, Alexander J. Dickson, and Andrey Bekker (Eds.)*
256 **Coastal Ecosystems in Transition: A Comparative Analysis of the Northern Adriatic and Chesapeake Bay** *Thomas C. Malone, Alenka Malej, and Jadran Faganeli (Eds.)*
257 **Hydrogeology, Chemical Weathering, and Soil Formation** *Allen Hunt, Markus Egli, and Boris Faybishenko (Eds.)*
258 **Solar Physics and Solar Wind** *Nour E. Raouafi and Angelos Vourlidas (Eds.)*
259 **Magnetospheres in the Solar System** *Romain Maggiolo, Nicolas André, Hiroshi Hasegawa, and Daniel T. Welling (Eds.)*
260 **Ionosphere Dynamics and Applications** *Chaosong Huang and Gang Lu (Eds.)*
261 **Upper Atmosphere Dynamics and Energetics** *Wenbin Wang and Yongliang Zhang (Eds.)*
262 **Space Weather Effects and Applications** *Anthea J. Coster, Philip J. Erickson, and Louis J. Lanzerotti (Eds.)*
263 **Mantle Convection and Surface Expressions** *Hauke Marquardt, Maxim Ballmer, Sanne Cottaar, and Jasper Konter (Eds.)*
264 **Crustal Magmatic System Evolution: Anatomy, Architecture, and Physico-Chemical Processes** *Matteo Masotta, Christoph Beier, and Silvio Mollo (Eds.)*
265 **Global Drought and Flood: Observation, Modeling, and Prediction** *Huan Wu, Dennis P. Lettenmaier, Qiuhong Tang, and Philip J. Ward (Eds.)*
266 **Magma Redox Geochemistry** *Roberto Moretti and Daniel R. Neuville (Eds.)*
267 **Wetland Carbon and Environmental Management** *Ken W. Krauss, Zhiliang Zhu, and Camille L. Stagg (Eds.)*
268 **Distributed Acoustic Sensing in Geophysics: Methods and Applications** *Yingping Li, Martin Karrenbach, and Jonathan B. Ajo-Franklin (Eds.)*
269 **Congo Basin Hydrology, Climate, and Biogeochemistry: A Foundation for the Future (English version)** *Raphael M. Tshimanga, Guy D. Moukandi N'kaya, and Douglas Alsdorf (Eds.)*
269 **Hydrologie, climat et biogéochimie du bassin du Congo: une base pour l'avenir (version française)** *Raphael M. Tshimanga, Guy D. Moukandi N'kaya, et Douglas Alsdorf (Éditeurs)*
270 **Muography: Exploring Earth's Subsurface with Elementary Particles** *László Oláh, Hiroyuki K. M. Tanaka, and Dezsö Varga (Eds.)*
271 **Remote Sensing of Water-Related Hazards** *Ke Zhang, Yang Hong, and Amir AghaKouchak (Eds.)*
272 **Geophysical Monitoring for Geologic Carbon Storage** *Lianjie Huang (Ed.)*
273 **Isotopic Constraints on Earth System Processes** *Kenneth W. W. Sims, Kate Maher, and Daniel P. Schrag (Eds.)*
274 **Earth Observation Applications and Global Policy Frameworks** *Argyro Kavvada, Douglas Cripe, and Lawrence Friedl (Eds.)*
275 **Threats to Springs in a Changing World: Science and Policies for Protection** *Matthew J. Currell and Brian G. Katz (Eds.)*
276 **Core-Mantle Co-Evolution: An Interdisciplinary Approach** *Takashi Nakagawa, Madhusoodhan Satish-Kumar, Taku Tsuchiya, and George Helffrich (Eds.)*
277 **Compressional Tectonics: Plate Convergence to Mountain Building (Tectonic Processes: A Global View, Volume 1)** *Elizabeth J. Catlos and Ibrahim Çemen (Eds.)*
278 **Extensional Tectonics: Continental Breakup to Formation of Oceanic Basins (Tectonic Processes: A Global View, Volume 2)** *Ibrahim Çemen and Elizabeth J. Catlos (Eds.)*
279 **Strike-Slip Tectonics: Oceanic Transform Faults to Continental Plate Boundaries (Tectonic Processes: A Global View, Volume 3)** *Ibrahim Çemen and Elizabeth J. Catlos (Eds.)*
280 **Landscape Fire, Smoke, and Health: Linking Biomass Burning Emissions to Human Well-Being** *Tatiana V. Loboda, Nancy H. F. French, and Robin C. Puett (Eds.)*
281 **Clouds and Their Climatic Impacts: Radiation, Circulation, and Precipitation** *Sylvia C. Sullivan and Corinna Hoose (Eds.)*
282 **Fast Processes in Large-Scale Atmospheric Models: Progress, Challenges, and Opportunities** *Yangang Liu and Pavlos Kollias (Eds.)*

Geophysical Monograph 282

Fast Processes in Large-Scale Atmospheric Models

Progress, Challenges, and Opportunities

Yangang Liu
Pavlos Kollias
Editors

Leo J. Donner
Advisor

This Work is a co-publication of the American Geophysical Union and John Wiley and Sons, Inc.

This edition first published 2024

Published under the aegis of the AGU Publications Committee

Matthew Giampoala, Vice President, Publications
Carol Frost, Chair, Publications Committee
For details about the American Geophysical Union visit us at www.agu.org.

Registered Office
John Wiley & Sons, Inc., 111 River Street, Hoboken, NJ 07030, USA

Editorial Office
111 River Street, Hoboken, NJ 07030, USA

For details of our global editorial offices, customer services, and more information about Wiley products visit us at www.wiley.com.

Wiley also publishes its books in a variety of electronic formats and by print-on-demand. Some content that appears in standard print versions of this book may not be available in other formats.

Library of Congress Cataloging-in-Publication Data

Names: Liu, Yangang, editor. | Kollias, Pavlos, editor. | Donner, Leo Joseph, 1956- other.
Title: Fast processes in large scale atmospheric models : progress, challenges, and opportunities / Yangang Liu, Pavlos Kollias, editors ; Leo J. Donner, advisor.
Description: Hoboken, NJ : Wiley-American Geophysical Union, 2024. | Series: Geophysical monograph series | Includes index.
Identifiers: LCCN 2023015913 (print) | LCCN 2023015914 (ebook) | ISBN 9781119528999 (cloth) | ISBN 9781119528968 (adobe pdf) | ISBN 9781119528944 (epub)
Subjects: LCSH: Atmospheric models.
Classification: LCC QC861.3 .F378 2024 (print) | LCC QC861.3 (ebook) | DDC 551.501/13–dc23/eng/20231012
LC record available at https://lccn.loc.gov/2023015913
LC ebook record available at https://lccn.loc.gov/2023015914

Cover image: © Guilherme Almeida da Silva/Getty Images
Cover design: Wiley

Set in 9.5/12pt TimesNewRomanMTStd by Straive, Chennai, India

CONTENTS

LIST OF CONTRIBUTORS

M. Joan Alexander
NorthWest Research Associates
Boulder, CO, USA

Vassilis Amiridis
Institute for Astronomy, Astrophysics, Space Applications and Remote Sensing
National Observatory of Athens
Athens, Greece

Julio T. Bacmeister
Climate and Global Dynamics Laboratory
National Center for Atmospheric Research
Boulder, CO, USA

Michael Barlage
National Center for Atmospheric Research
Boulder, CO, USA

Alexei Belochitski(†)
I. M. Systems Group
Environmental Modeling Center
College Park, MD, USA

Kamal Kant Chandrakar
National Center for Atmospheric Research
Boulder, CO, USA

Fei Chen
National Center for Atmospheric Research
Boulder, CO, USA

Anthony B. Davis
NASA Jet Propulsion Laboratory
California Institute of Technology
Pasadena, CA, USA

Xiquan Dong
Department of Hydrology and Atmospheric Sciences
University of Arizona
Tucson, AZ, USA

Leo J. Donner
NOAA Geophysical Fluid Dynamics Laboratory
Princeton University
Princeton, NJ, USA

Graham Feingold
Chemical Sciences Laboratory
NOAA Earth System Research Laboratories
Boulder, CO, USA

Sinan Gao
Collaborative Innovation Center on Forecast and Evaluation of Meteorological Disasters / Key Laboratory for Aerosol-Cloud-Precipitation of China Meteorological Administration
Nanjing University of Information Science and Technology
Nanjing, China

Virendra P. Ghate
Environmental Science Division
Argonne National Laboratory
Lemont, IL, USA

Yu Gu
Joint Institute for Regional Earth System Science and Engineering, and Department of Atmospheric and Oceanic Sciences
University of California Los Angeles
Los Angeles, CA, USA

Christopher Heale
Department of Physical Sciences
Embry–Riddle Aeronautical University
Daytona Beach, FL, USA

Pavlos Kollias
Environmental and Climate Sciences Department
Brookhaven National Laboratory
Upton, NY, USA
and
School of Marine and Atmospheric Science
Stony Brook University
Stony Brook, NY, USA

Ilan Koren
Department of Earth and Planetary Sciences
Weizmann Institute
Rehovot, Israel

Vladimir Krasnopolsky
Environmental Modeling Center/National Centers for Environmental Predictions/National Weather Service
NOAA Center for Weather and Climate Prediction
College Park, MD, USA

Christopher G. Kruse
NorthWest Research Associates
Boulder, CO, USA

Marcin J. Kurowski
NASA Jet Propulsion Laboratory
California Institute of Technology
Pasadena, CA, USA

Katia Lamer
Department of Environmental and Climate Sciences
Brookhaven National Laboratory
Upton, NY, USA

Vincent E. Larson
Department of Mathematical Sciences
University of Wisconsin–Milwaukee
Milwaukee, WI, USA
and
Pacific Northwest National Laboratory
Richland, WA, USA

Wuyin Lin
Department of Environmental and Climate Sciences
Brookhaven National Laboratory
Upton, NY, USA

Alexander Marshak
NASA Goddard Space Flight Center
Greenbelt, MD, USA

Kuo-Nan Liou(†)
Joint Institute for Regional Earth System Science and Engineering, and Department of Atmospheric and Oceanic Sciences
University of California Los Angeles
Los Angeles, CA, USA

Xiaohong Liu
Department of Atmospheric Sciences
Texas A&M University
College Station, TX, USA

Yangang Liu
Environmental and Climate Sciences Department
Brookhaven National Laboratory
Upton, NY, USA

Ulrich Loehnert
Institute of Geophysics and Meteorology
University of Cologne
Cologne, Germany

Chunsong Lu
Collaborative Innovation Center on Forecast and Evaluation of Meteorological Disasters / Key Laboratory for Aerosol-Cloud-Precipitation of China Meteorological Administration
Nanjing University of Information Science and Technology
Nanjing, China

Eleni Marinou
Institute for Astronomy, Astrophysics, Space Applications and Remote Sensing
National Observatory of Athens
Athens, Greece

Allison McComiskey
Department of Environmental and Climate Sciences
Brookhaven National Laboratory
Upton, NY, USA

David B. Mechem
Department of Geography and Atmospheric Science
University of Kansas
Lawrence, KS, USA

Patrick Minnis
Analytical Mechanics Associates, Inc.
Hampton, VA, USA

Jadwiga H. Richter
Climate and Global Dynamics Laboratory
National Center for Atmospheric Research
Boulder, CO, USA

Sabrina Schnitt
Institute of Geophysics and Meteorology
University of Cologne
Cologne, Germany

Raymond A. Shaw
Atmospheric Sciences Program
Michigan Technological University
Houghton, MI, USA

Cheng Sun
Collaborative Innovation Center on Forecast and Evaluation of Meteorological Disasters / Key Laboratory for Aerosol-Cloud-Precipitation of China Meteorological Administration
Nanjing University of Information Science and Technology
Nanjing, China

Kay Suselj
NASA Jet Propulsion Laboratory
California Institute of Technology
Pasadena, CA, USA
and
Joint Institute for Regional Earth System Science and Engineering
University of California Los Angeles
Los Angeles, CA, USA

João Teixeira
NASA Jet Propulsion Laboratory
California Institute of Technology
Pasadena, CA, USA
and
Joint Institute for Regional Earth System Science and Engineering
University of California Los Angeles
Los Angeles, CA, USA

Junhong Wei
School of Atmospheric Sciences and Guangdong Province Key Laboratory for Climate Change and Natural Disaster Studies
Sun Yat-sen University
Guangzhou, China
and
Southern Marine Science and Engineering Guangdong Laboratory
Zhuhai, China

Shaocheng Xie
Atmospheric, Earth and Energy Division
Lawrence Livermore National Laboratory
Livermore, CA, USA

Xiaoqi Xu
Collaborative Innovation Center on Forecast and Evaluation of Meteorological Disasters / Key Laboratory for Aerosol-Cloud-Precipitation of China Meteorological Administration
Nanjing University of Information Science and Technology
Nanjing, China

PREFACE

Computer models are essential tools for understanding atmospheric phenomena and for making accurate predictions of any changes in the Earth's climate, weather, and resources of renewable energy resulting from anthropogenic activities that generate greenhouse gases and particulates into the atmosphere. Many physical processes that influence Earth's climate and weather occur on spatial (temporal) scales smaller (shorter) than typical grid sizes (time steps) of general circulation models, and thus must be parameterized.

This book focuses on the atmospheric subgrid processes—collectively called fast physics—by reviewing and synthesizing relevant physical understanding, parameterization developments, various measurement technologies, and model evaluation framework. The book contains 18 chapters and is divided into three parts to reflect and synthesize the multiple aspects involved.

The first chapter briefly introduces the historical development of fast physics parameterizations and the involved complexities. Part I is devoted to discussing major subgrid processes, with eight chapters (Chapters 2–9) each covering different processes more or less in the conventional compartmentalized format that emphasizes individual processes. Topics covered include, but not limited to, radiative transfer, aerosols, and aerosol direct and indirect effects; entrainment-mixing processes and their microphysical influences; convection and convective clouds; stratiform clouds such as stratus and stratocumulus; planetary boundary layer processes; land surface and its interactions with the atmosphere; and gravity waves. On top of the conventional treatments, some promising ideas/approaches are described that have recently emerged to unify the treatment of individual processes and thus allow for consideration of process interactions.

Part II is devoted to such unifying efforts, with four chapters (Chapters 10–13) covering four different endeavors: the unifying parameterizations based on assumed probability density functions; the EDMF approach that combines the eddy–diffusivity and mass–flux approaches to unify turbulence and convection; application of machine learning techniques; and innovative top-down attempts that consider the involved totality by borrowing ideas from systems theory, statistical physics, and nonlinear sciences.

Part III (Chapters 14–17) is devoted to assessments, model evaluation, and model-measurement integration, with four chapters that focus on satellite and airborne remote-sensing measurements; surface-based remote-sensing measurements; in situ and laboratory measurements; and model evaluation and model-measurement integration, respectively. The final chapter of the book summarizes emerging challenges, new opportunities, and future research directions.

The development of the book happened around two noteworthy events. The first was that the 2021 Nobel Prize in Physics was awarded to three pioneers in modeling climate and weather and studying complex systems (Syukuro Manabe of Princeton University, USA; Klaus Hasselmann of the Max Planck Institute for Meteorology, Germany; and Giorgio Parisi of Sapienza University of Rome, Italy). This exciting choice accentuates not only the critical importance of the subject but also the outstanding challenges of the topics discussed in this book.

The second event was the COVID-19 pandemic, which unfortunately overlapped with the writing of most of the chapters in this book and affected the lives of many of our contributors. We would like to express our special thanks to all the authors and reviewers, as well as to the staff at Wiley and AGU for their hard work and patience as we completed this book under these circumstances.

This book is dedicated to two of our dear colleagues and contributing authors who passed away during this period, Kuo-Nan Liou and Alexei Belochitski. The book is also dedicated to Yangang Liu's mother, Chunlan Sun, who was hospitalized during the pandemic and passed away in China recently without his company.

Yangang Liu
Brookhaven National Laboratory, USA
Pavlos Kollias
Brookhaven National Laboratory, USA
and Stony Brook University, USA

1

Progress in Understanding and Parameterizing Fast Physics in Large-Scale Atmospheric Models

Yangang Liu[1] **and Pavlos Kollias**[1,2]

ABSTRACT

This introductory chapter discusses the atmospheric subgrid processes – collectively called "fast physics" or "fast processes" – and their parameterizations in large-scale atmospheric models. It presents a brief historical progression of the parameterization of fast processes in numerical models. Despite great efforts and notable advances in understanding, progress in improving fast physics parameterizations has been frustratingly slow, the underlying reasons for which are explored. To guide readers, this chapter describes the main objectives and scope of this book and summarizes each chapter.

1.1. FAST PHYSICS AND PROGRESS OF PARAMETERIZATION DEVELOPMENT

Large-scale atmospheric models are integral components of weather and climate models. Ongoing developments in high-resolution modeling (i.e., global storm-resolving models (GSRMs; Stevens et al., 2019); Energy Exascale Earth System Model (E3SM; Rasch et al., 2019); and large-eddy simulations (LES; Gustafson et al., 2020)) have resulted in ultra high-resolution numerical simulations of atmospheric systems. Despite these advancements, coarser resolution large-scale models remain our main modeling capability for future climate predictions. Many atmospheric processes and phenomena that influence Earth's weather and climate occur at spatiotemporal scales that are too small to be resolved in these large-scale atmospheric models and must be parameterized – approximately represented by the variables that can be resolved by the model grids. In this book, we refer to this array of parameterized subgrid processes and phenomena collectively as "fast physics" or "fast processes" for convenience, including radiative transfer, aerosol/cloud physics, convection, boundary layer processes, gravity wave (GW), and land-atmosphere interactions.

While early parameterizations of fast physics used simple and often empirical or ad hoc relationships (e.g., the Kessler bulk parameterization for representing cloud microphysical processes; Kessler, 1969), later parameterization development was concerned about building conceptual models with increasingly detailed physical processes by leveraging theoretical analysis, observations, and/or detailed process modeling studies.

Furthermore, parallel to the continuing improvement/development of parameterizations for individual fast processes, there has been growing interest in studying and understanding interactions/couplings among different processes. Significant progress has been made and several promising approaches have emerged since late 1900s and early 2000s. Figure 1.1 illustrates the approximate timelines in developing fast physis parameterizations in context of the conventional parameterizations that target individual processes as well as several unifying efforts that addresses multiple processes together.

[1] *Environmental and Climate Sciences Department, Brookhaven National Laboratory, Upton, NY, USA*

[2] *School of Marine and Atmospheric Sciences, Stony Brook University, Stony Brook, NY, USA*

Fast Processes in Large-Scale Atmospheric Models: Progress, Challenges, and Opportunities, Geophysical Monograph 282, First Edition.
Edited by Yangang Liu and Pavlos Kollias.

DOI: 10.1002/9781119529019.ch01

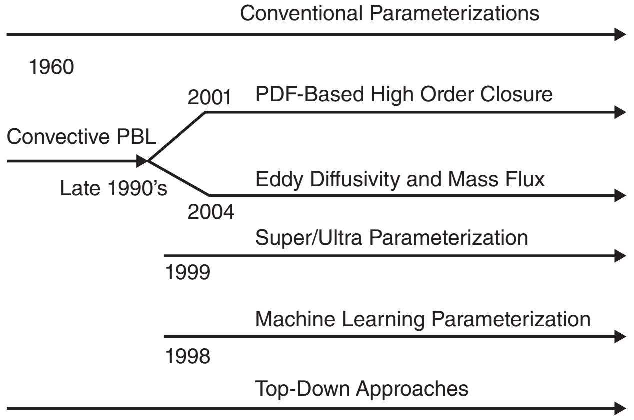

Figure 1.1 Schematic of the approximate timelines of development of fast physics parameterizations. Conventional parameterizations are focused on individual fast processes. The four lines of unifying efforts (PDF-Based High Order Closure, Eddy Diffusivity and Mass Flux, Super/Ultra Parameterization, and Machine Learning Parameterization) aim to unify the representation of more than two physical processes. Top-down approaches borrow holistic ideas that have been scattered in various disciplines (e.g., nonlinear systems dynamics, statistical physics, information theory, self-organization, networks, and pattern formation).

Despite remarkable efforts and increasing recognition of the importance of these fast processes over the past few decades, progress remains frustratingly slow in improving their representation in models. As a result, their impacts on future climate predictions remain poorly understood and highly uncertain. The slow progress is perhaps best attested by the historical lack of change in the ranges of climate sensitivity across models from the celebrated 1979 US National Research Council report (Charney et al., 1979) to the latest (6th) Coupled Model Intercomparison Project (CMIP6) results used in the Intergovernmental Panel on Climate Change (IPCC) report (Figure 1.2). Deficient fast physics parameterizations, especially those related to clouds, have been thought to be primarily responsible for the stubborn large spread of model climate sensitivity (Meehl et al., 2020; Zelinka et al., 2020). Aerosol climate forcing in climate models has been fraught with similarly unchanged uncertainty (for details refer to Chapter 3 of this book).

The slow progress can be attributed to two overarching types of complexities (also see Jakob, 2010; Randall, 2013). The first lies in the "4M-2N complexities" inherently accompanying the atmosphere and associated physical processes (Figure 1.3). Briefly, fast processes and especially those cloud-related ones involve *multibody* (sub)systems with numerous particles of different sizes and shapes, in which multiple physical processes (*multiphysics*) occur over a wide range of spatiotemporal scales (*multiscale*) and interact with one another, and manifest themselves in a variety of cloud types such as cumulus and stratiform clouds (*multitype*). The equations describing these processes are often highly *nonlinear* and exhibit *non-Gaussian* statistics (Lovejoy & Schertzer, 2010).

The other inherent complexity lies with that model development involves an iterative cycle of developing parameterizations, implementing and evaluating parameterizations against observations to identify potential parameterization deficiencies and further improvement. This iterative procedure calls for an organic integration of

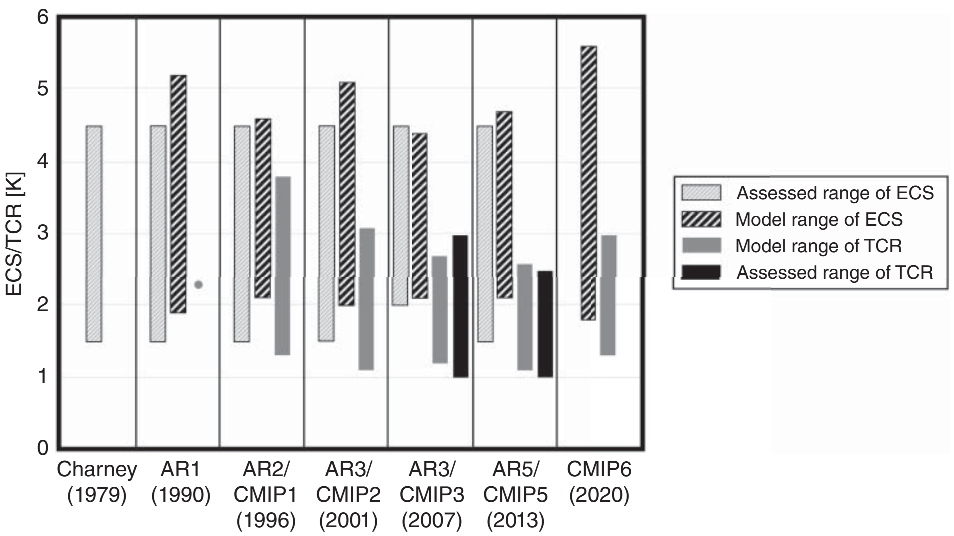

Figure 1.2 Historical values of equilibrium climate sensitivity (ECS) and transient climate response (TCR). Source: Adapted from Meehl et al. (2020), which can be consulted for details on the data sources and definitions.

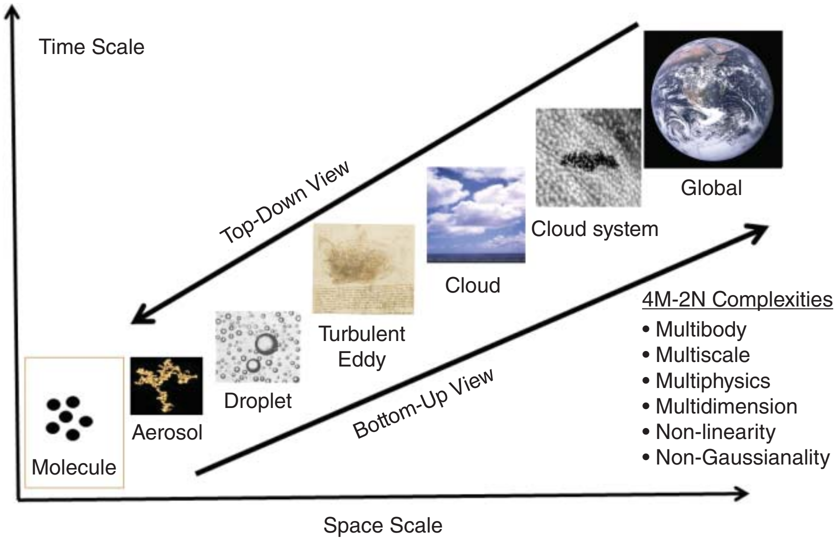

Figure 1.3 Schematic to illustrate the atmospheric scale hierarchy and involved "4M-2N complexities." Together with the "operational complexity" discussed in the text, these science complexities have posed and will continue to pose challenges to model development in general and fast physics parameterizations in particular. Source: Leonardo da Vinci/Wikimedia Commons and NASA/Wikimedia Commons/Public Domain.

the key components involved ranging from modeling to measurements, which in turn demands effective coordination of expertise in distinct areas. However, effective coordination and collaboration across different disciplines and institutions are not trivial, and such an "operational complexity" adds another layer of technological and social challenges in virtually every step of model development. The issue will become more acute as the field is moving toward more emphasis on process interactions with ever-increasing data volumes and model resolutions. To echo Jakob (2010), "… acceleration in model development can only be achieved by significantly strengthening these weak links through additional research and better coordination across existing programs."

1.2. OBJECTIVES AND SCOPE OF THE BOOK

The objectives of this book are threefold. First, to survey advances in understanding of key fast processes and their parameterization developments (Part I). In particular, Part II of this book is uniquely devoted to unifying efforts. Second, unlike most review articles or the book by Stensrud (2007) on fast physics parameterizations, this book includes discussions on measurement techniques and studies that use observations for model evaluation and thus covers approaches to addressing the weak link in the iterative loop of model development. Third, by surveying the recent advances in key areas, we hope to reveal new challenges, opportunities, and directions for future research.

It is worth noting that the related literature is enormous and that the selection of the material in this text is nonexhaustive and likely biased to the authors' own research interests. On the other hand, books focusing on fast physics parameterizations are rare; the only one we are aware of is Stensrud (2007), which is primarily on conventional parameterizations of individual fast processes in numerical weather prediction (NWP) models. Bringing together modeling and measurements with a common goal of parameterization development and evaluation and including multiple unifying efforts are unique to this book.

1.3. BOOK STRUCTURE AND SUMMARY OF CHAPTERS

Fast physics in large-scale atmospheric models involves multiple processes that occur over a wide range of spatiotemporal scales. Progress has been made on many fronts and new promising directions of research are emerging. To reflect and synthesize the multiple facets involved, this book is divided into three parts. Part I deals with the major subgrid processes, with eight chapters (Chapters 2–9) covering different fast processes. Beyond conventional treatments, some promising approaches have recently emerged to unify the treatment of (some) processes and thus allows for consideration of process interactions. Part II is devoted to such unifying efforts, with four chapters (Chapters 10–13) that each cover a different endeavor. Part III is devoted to measurements, model evaluation, and model-measurement integration, with four chapters (Chapters 14–17) that focus on satellite and airborne remote sensing measurements, surface-based remote sensing measurements, in situ and laboratory measurements, and model evaluation and model-measurement integration, respectively.

1.3.1. Process Studies and Parameterizations

Essential to the Earth's climate and weather and understanding climate change is the understanding and representation of the solar (shortwave) and terrestrial (longwave) radiation and of radiative transfer processes such as absorption, and scattering. In Chapter 2, Gu and Liou present the fundamentals of radiative transfer and its interactions with the atmosphere, and summarize the commonly used radiative transfer parameterization schemes in atmospheric models. Also discussed are several more advanced topics in the study of the atmospheric radiation, including cloud vertical overlapping, cloud horizontal inhomogeneity, and 3D radiative transfer in both the cloudy atmosphere and over complex rugged land surfaces such as mountainous terrains. In particular, the chapter highlights that the current commonly used radiation schemes normally represent 1D transport in the vertical direction, although radiative transfer in 3D atmosphere and surfaces could play an important role in determining the radiation budget and radiative heating at the top of the atmosphere, at the surface, and within the atmosphere. Both horizontal and vertical subgrid scale inhomogeneities and 3D radiative transfer may substantially influence the radiative transfer within clouds and cloud-radiation interactions, suggesting the need for further investigation and for improving their representations in models.

Atmospheric aerosols are suspensions of solid particles or liquid droplets in the air. Aerosols contain multiple compositions, exhibit various morphologies, and span a few orders of magnitude in sizes from a few nanometers to tens of micrometers. Aerosol radiative effects constitute one of the largest uncertainties in climate projection, and the large spread of simulated values among general circulation models (GCMs) can be traced to different representations of aerosol processes, including emissions, transport, formation and removal, and aerosol-cloud interactions. In Chapter 3, Liu provides an overview of atmospheric aerosols and their climatic impacts through both aerosol direct effects on radiation (aerosol-radiation interactions) and aerosol indirect effects (aerosol-cloud interactions). The authors focus on addressing topics related to three aerosol-related questions: (1) How are aerosol properties and processes as well as aerosol-cloud interactions represented and compared in current GCMs? (2) What are the major assumptions, simplifications, and weaknesses of the current representations? (3) Why are there large uncertainties in the aerosol climate effects from GCMs? Several future directions are highlighted.

Although entrainment of surrounding dry air into clouds, subsequent turbulent mixing processes, and their microphysical influences have been known to be essential in determining cloud microphysical and related properties for some time, theoretical understanding of these processes is still far from complete, and their parameterizations in atmospheric models are in their infancy. In Chapter 4, Lu, Liu, Xu, Gao, and Sun discuss these issues in shallow clouds (cumulus and stratocumulus clouds), focusing on two critical yet understudied aspects: entrainment-mixing mechanisms and entrainment rate. Different conceptual models of entrainment-mixing mechanisms are reviewed, and latest studies on unifying microphysical measures to quantify different entrainment-mixing mechanisms are presented. Approaches for estimating fractional entrainment rate in cumulus clouds are summarized; relationships of entrainment rate to internal cloud properties (e.g., vertical velocity) or external properties (e.g., relative humidity in environment) are discussed as plausible parameterizations. Three approaches for estimating entrainment velocity in stratocumulus clouds are also discussed. Several topics are highlighted for future research, e.g., the connection between entrainment rate, entrainment-mixing mechanisms, and relationships to other factors (e.g., rain initiation, detrainment, spectral shape of cloud droplet size distributions, entrained aerosols, and environmental relative humidity).

Following the discussion on entrainment in shallow cumulus clouds and its role in shallow convection parameterization, Donner turns to deep convection from the perspective of large-scale flows in Chapter 5. The chapter begins with discussing the effects of convection on large-scale flows in which it is embedded, follows with strategies for solving the problem of cumulus parameterization, and concludes with a brief overview of interactions between convection and momentum, chemistry, tracers, cloud microphysics, and aerosols. Emphasized are the roles of convective vertical velocities in treating aerosol-cloud interactions and cloud microphysics related to cloud feedbacks. Major deficiencies in existing parameterizations are discussed, including interactions between deep convection and aerosols, convection-chemistry interactions, understanding and representation of convective organization, and knowledge of convective-scale pressure-gradient forces in treating effects of convection on momentum fluxes. Limitations of mean-state perspectives and the widely used quasi-equilibrium assumption are discussed. Also touched on are connections with other topics (e.g., scale awareness, higher-order closure, multiscale modeling frameworks and high-resolution models without conventional deep convection parameterizations, shallow convection, boundary-layer processes, and gravity waves) detailed in other chapters.

Besides convective clouds, stratiform clouds including stratus and stratocumulus clouds constitute another critical component of the atmospheric system that significantly affects climate and has long been the subject of active research from many perspectives. In Chapter 6, Dong and Minnus provide an overview of such clouds, with a focus on what we have learned from observational studies in terms of improving their parameterization in atmospheric models. Stratus and stratocumulus cloud properties and their importance are discussed based on measurements from trained surface observers, satellite and ground-based remote sensors, and aircraft field campaigns. The processes that determine the variations in stratocumulus properties and govern where and when they occur are discussed, along with such factors as aerosols, radiation, and humidity. Retrieval methods used for extracting information about stratus and stratocumulus clouds from satellite- and ground-based sensors are also briefly reviewed, with an emphasis on the knowledge learned for improving understanding and parameterizations of such clouds in large-scale models. Unique consistency between the early trained observers and the state-of-the-art technologies is demonstrated; synergy of different observational platforms is highlighted for future investigation. Emerging but understudied phenomena are summarized, including the impact of low-level temperature advection, veil clouds developing at the top of the marine boundary layer in areas of open-cell and unorganized cellular convection, the role of gravity waves in the subtropical jet stream in initiating Pocket of Cells in some closed-cell stratocumulus over the southeast Pacific, and effects of land-sea breezes. Outstanding issues in profiling marine boundary layer cloud and drizzle microphysical properties are highlighted, including the need for incorporating cloud-top entrainment, drizzle, and vertical and horizontal inhomogeneities to address the issue of nonadiabatic multispectral retrievals.

As a layer between the ground surface and the free troposphere, the planetary boundary layer (PBL) is often turbulent and particularly important, because the majority of biota (including humans) and climatically important low clouds like stratocumulus and shallow cumulus reside. Even deep convection is highly related to the properties of the plumes or thermals originating in the PBL. In Chapter 7, Ghate and Mechem introduce the PBL structure and the commonly used theoretical approaches for investigating the PBL. A hierarchy of models for representing the boundary layer is presented, including mixed-layer models, first-order closure, 1.5-order TKE closure, and higher-order closure approaches. Challenges for evaluating the emerging advanced schemes (high order, PDF-based, or EDMF) are also discussed in context of the inherent needs for observations of joint PDFs of vertical air motion and thermodynamic variables. The discussion emphasizes the buoyancy-driven convective boundary layer but briefly mentions impacts of shear and clouds. The chapter concludes with a brief historical context and future outlook for representing the boundary layer in large-scale atmospheric models. To some extent, this chapter can be viewed as an introduction to Chapters 13 and 14 where the PDF-based and EDMF schemes are detailed.

Although the focus of this book is on atmospheric processes, the weather and climate system consists of other subsystems that strongly interact with the atmosphere over a wide range of spatiotemporal scales. In particular, various surface processes are fundamental to the exchange of heat, water, and momentum between the surface and the atmosphere through PBL. Thus, modeling land-surface processes has been an integral component of atmospheric models. In Chapter 8, Barlage and Chen focus on recent progress in understanding and modeling the biophysical effects of the human dimension, especially urbanization and agriculture, on surface water and energy budgets, and their cascading effects on weather and climate including clouds, aerosols, convection, and precipitation. Well-known phenomena are discussed, including the Urban Heat Island and urban impacts on precipitation through both cloud microphysical and/or dynamical effects. Also discussed are the unique roles of rough vegetated or urban canopy in determining turbulent fluxes (e.g., evapotranspiration over vegetated regions can exceed evaporative flux from the oceans because of larger surface roughness and stronger turbulence whereas the moisture flux can be effectively shut off when the land is dry). Land-surface models (parameterizations) of 3D subgrid structures within urban or vegetation canopies are presented, including the most sophisticated multilayer scheme – Building Effect Parameterization. Challenges for evaluating and applying such a comprehensive land-surface model are discussed, including existence and specification of the large number of tunable parameters used in urban canopy models.

Atmospheric GWs have horizontal wavelengths ranging from 1 to thousands of kilometers. Current climate models and even NWP models cannot resolve significant portions of their momentum flux, and parameterizations are necessary to represent their under- or unresolved effects in atmospheric models. In Chapter 9, Kruse, Richter, Alexander, Bacmeister, and Wei discuss GWs that are important at nearly all levels of the atmosphere, especially for the general circulation of the middle and upper atmosphere. GWs in the tropical stratosphere significantly contribute to the driving of the quasi-biennial oscillation and the stratospheric and mesospheric semiannual oscillation, both primary modes of variability up there. In the extratropics, GWs contribute to the driving of the stratospheric Brewer-Dobson circulation and significantly influence the strength of the polar night jet and the corresponding polar temperatures. Additionally, GWs are responsible for the cold summer mesopause and the reversal of extratropical zonal mean winds in the mesosphere. Also discussed are both primary sources of atmospheric GWs (i.e., flows over mountains, moist convection, and imbalances in jets and frontal systems) and secondary GWs generated as a result of dissipation of primary GWs. The basic theory of GW generation, propagation, and dissipation and commonly used GW parameterizations are presented. Uncertainties, parameter tuning, and known missing processes in current parameterizations are explored as well. The importance of gravity wave in shaping clouds (Chapter 7) and in determining cloud microphysical properties (Chapter 3) is gradually recognized as well.

1.3.2. Unifying Efforts

Chapter 10 is the first of the four chapters that introduce the emerging efforts to unify the parameterizations of different processes, with a focus on higher-order equations closed by assuming the shape of the probability density function (PDF) of fields on the subgrid scale (PDF-based method for short). In this chapter, Larson presents the general equations involved. Theoretical analysis of the higher-order equations reveals that they contain the flux-of-flux terms that lead to nonlocal cumulus transport, along with a detailed representation of buoyant generation of turbulence, which is the essential source term of convection and can be closed by a multivariate PDF. Instead, traditional low-order closure omits the flux-of-flux terms that are crucial for representing nonlocal cumulus transport. The popular Cloud Layers Unified By Binormals (CLUBB) is detailed as an example of such PDF-based methods. Other higher-order closure models are also briefly discussed, including the Intermediately Prognostic Higher-Order Closure (IPHOC) parameterization (Cheng et al., 2010) and the Turbulence Kinetic Energy-Scalar Variance (TKESV) parameterization of Mironov and Machulskaya (2017). The IPHOC prognoses all the moments prognosed by CLUBB, plus two additional third-order moments of water vapor and potential temperature; TKESV prognoses TKE and scalar variances, and optionally a third-order moment related to cloud liquid water. The connections of the PDF-based method to the conventional mass-flux method for convection and low-order closure for turbulence are also discussed.

Another approach that seeks to unify the treatment of convection and turbulent processes in PBL is conceptually more direct, combining the widely used eddy diffusivity approach for local turbulent transport with the mass-flux scheme for convection. In Chapter 11, Teixeira, Suselj, and Kurowski discuss the EDMF approach. After briefly reflecting on the early development in the late 1990s, this chapter focuses on the new stochastic multiplume EDMF scheme that can realistically represent the dry boundary layer, stratocumulus, shallow, and even deep cumulus convection within a single framework. The variability of updraft properties is parameterized using joint PDFs of thermodynamic properties to initialize multiple updrafts. Lateral entrainment is parameterized as a stochastic process. Furthermore, the unified EDMF parameterization explicitly considers the horizontal resolution of the model, paving the way to a scale-aware extension of the scheme. Both the fundamentals and latest results of using the new EDMF scheme are introduced. The multiplume framework allows for the coexistence of different convective regimes (i.e., dry plumes, shallow moist convection, and even deep convection) within a single grid box, without any artificial separations between them and with scale-adaptive capabilities for use in next-generation weather and climate models with high and variable horizontal resolutions.

The PDF-based and EDMF approaches both aim to unify the parameterizations of turbulence, PBL, and convection (especially shallow convection). Further coupling with other processes such as cloud microphysics remains an area of active research for both approaches. Around similar times in the late 1990s and early 2000s, ideas of superparameterization – that embed cloud-resolving models (CRM) in climate model grid column – were proposed and developed as a way to replace all the subgrid processes that the embedded CRM model represents, including turbulence, PBL, convection, cloud microphysics, and radiation (Grabowski, 2001; Randall, 2013). Recently, similar ideas were extended to using high-resolution LES models instead of CRMs in so-called ultraparameterization (Parishani et al., 2017). Obviously, the benefits of such multiscale modeling approaches come at high computational cost and call for more computationally effective approaches that can be used as alternative to represent multiple fast processes together. Note that even for LES models, many sub-LES processes such as cloud microphysics and turbulence-microphysics interactions remain to be parameterized (Liu et al., 2023). In Chapter 12, Krasnopolsky and Belochitski describe applications of machine learning (ML) approaches to emulate existing parameterizations and developing new ML surrogate models as new parameterizations. The authors first argue that a parameterization can be formulated as a generic problem of mathematical mapping and then argue that ML tools can be used to emulate and/or approximate the involved mathematical mappings. Four mapping complexities (physical complexity, mathematical complexity, numerical/computational complexity, and functional complexity) are discussed. Further discussed are ML applications to emulate existing parameterizations, to develop new parameterizations, to ensure physical constraints, and to control the accuracy of developed applications. Some ML approaches that allow developers to go beyond the standard parameterization paradigm are discussed as well. Limitations of ML models are also discussed, including inability to provide a meaningful physical interpretation of underlying processes, requirements of large data for training and testing purposes, and their limited generalizability to out-of-sample scenarios. Given that neither an ML-only nor a physically based-only approach can be considered sufficient for complex scientific and engineering applications, the research community has been exploring the hybridization of physically based and ML-based models, where both scientific knowledge and data are integrated in a synergistic manner. It is reasoned that this hybrid paradigm is fundamentally different from the ML mainstream where domain-specific knowledge is often considered secondary, and several differences are discussed. The concept of compound parameterization that combines an ML parameterization, the original physically based parameterization, and a quality control procedure is introduced.

Despite the tremendous advances and different extents in dealing with the number of fast processes and their interactions discussed in the previous chapters, a common theme of those studies is that they are all essentially bottom-up-based and aim to upscale subgrid scale processes to grid variables. However, the climate system, including its atmospheric component, is a multiscale complex system that involves highly nonlinear bottom-up and top-down scale interactions (recall Figure 1.3). Without considering the top-down direction, our understanding would never be complete, and the physical pictures from the unifying efforts could be as murky as understanding the output of a full GCM. As another unique addition of this book compared to existing ones, in Chapter 13, Feingold and Koren summarize innovative ideas that attempt to consider processes holistically but are scattered in various disciplines including nonlinear dynamics (e.g., chaos theory), statistical physics, information theory, self-organization, networks, pattern formation, and general systems theory. The "top-down view" is focused on system-wide behavior and emergent phenomena, distinguishing from the traditional "bottom-up" view that focuses on individual processes. In particular, a new behavior at a larger scale can emerge from interactions/couplings between detailed processes and between the involved subsystems at a finer scale. And this type of order/emergence is not driven by an external force, but instead grows spontaneously from local interactions, or is "self-organized." Spatiotemporal communication between components of a system is key to development of synchronization, patterns, and self-organization. It is argued that the top-down approach can yield simple holistic models that are more amenable to interrogation and digestion than complex, detailed models. Concepts and terminologies that are not familiar to the atmospheric modeling, especially the parameterization and community, are introduced and discussed, including fixed points, attractors, limit cycles, chaotic state, bifurcation points, synchronization, information content, and entropy. In addition to their distinct foci on local and detailed physical processes vs. process interactions and emergence, this chapter also provides some intriguing examples to elucidate the conceptual differences between the bottom-up and top-down approaches from other perspectives: reductionism vs. holism; basic building blocks vs. integrative view; models representing a large vs. a reduced number of degrees of freedom; models rooted in mathematical representation of physical/chemical/biological processes vs. models that are an abstraction of these processes; and complexity vs. simplicity. The authors use aerosol-cloud-precipitation system as a particular example to demonstrate the great potentials of the top-down view and the need to integrate the complementary top-down view and bottom-up thinking in addressing the remaining challenge.

1.3.3. Measurements, Model Evaluation, and Model-Measurement Integration

Reliable observations are always important to improve our understanding of natural phenomena including atmospheric processes and serve as the ground truth to verify and evaluate any theoretical and modeling developments. The synergy between model development and observations is becoming increasingly important as both fields progress. Earth science observations in general and atmospheric observations in particular have unique features, involving different but complementary approaches: surface-based, satellite-based and airborne remote sensing, in situ field measurements, and laboratory studies. This part is devoted to such crucial endeavors, with four chapters focusing on four different topics that are summarized next.

Chapter 14 focuses on surface-based remote sensing for the study of the macrophysical and microphysical structure of clouds, precipitation, aerosols, and PBL. In this chapter, Lamer, Kollias, Amiridis, Arinou, Loehnert, Schnitt, and McComiskey place their emphasis on the unique ability of ground-based system to continuously characterize the atmosphere at high vertical resolution from near the surface to the top of the atmosphere, effectively filling observational gaps left by spaceborne and aircraft platforms. Following an overview of the emergence of ground-based observatories, details about the measurement principles of some cornerstone instruments (e.g., cloud and precipitation radars, lidars, and radiometers) are provided. Modern techniques to retrieve cloud and precipitation location, microphysical and dynamical properties, as well as PBL structure and aerosol properties are discussed, including their underlying assumptions and uncertainties. Several challenges associated with using ground-based observations for model evaluation are discussed. For example, most measurements are related to moments of particle size distributions (e.g., the 6th and 2nd being recorded by radars and lidar, respectively), which differ from those of most interest in models (e.g., the 0th moment for particle number concentration and 3rd moment for mass content). Furthermore, high-resolution observations and large-scale models involve widely different scales; GCMs having grid resolutions larger than 50 km, while radars have a range resolution of ~30 m. The growing role of synthetic Observing Systems Simulation Experiments (OSSEs), instrument simulators, and subcolumn generators in bridging those gaps is emphasized. The chapter concludes with an outlook on the next generation of ground-based observatories that should employ scanning systems and distributed networks.

In Chapter 15, Marshak and Davis cover remote sensing of cloud and aerosol properties from overhead instruments, including satellite-based and airborne sensors with standoff distances ranging from NASA's P-3B aircraft at about 3.5 km above cloud top to the Deep Space Climate Observatory (DSCOVR) platform at the Lagrange-1 point, about 1,500,000 km toward the Sun. The electromagnetic spectrum covered ranges from the ultraviolet to microwaves, and both traditional passive and relatively recent active (e.g., lidar and radar) and modalities are discussed. The emphasis is on the physics behind the sensors as well as on the retrieval algorithms. The chapter starts with remote sensing of cloud properties, introducing the popular Nakajima-King approach widely used in retrievals of cloud optical depth and particle size and the Bréon-Goloub approach that is based on the directional signature of the polarized reflectance. Techniques for retrieving cloud properties (mostly ice) with microwave sensors are also briefly described. The chapter then switches to remote sensing of aerosol properties, describing the main aerosol remote sensing approaches used by the major satellite imagers. In addition to passive remote sensing, the active remote sensing methods for aerosol and cloud profiling are also highlighted, with an emphasis on CALIPSO and CloudSat for lidar and radar, respectively. The chapter explores oxygen A-band and B-band remote sensing of cloud and aerosol layer height, along with other passive methods for estimating cloud top height. A special section is dedicated to cloud remote sensing at very high spatial resolution either from tasked imaging sensors in space or from airborne platforms deployed above the clouds of interest, such as NASA's ER-2. New studies on the transition zone are reviewed. The chapter closes with a brief discussion of retrieval uncertainty quantification for both cloud and aerosol remote sensing.

Laboratory experiments allow more controlled, repeatable measurements of a physical quantity or phenomenon in a well-defined system of interest with known external influences. In Chapter 16, Chandrakar and Shaw describe in situ measurements and laboratory experiments, with a focus on physical processes that are small in spatial or temporal scale such as cloud microphysics and small-scale turbulence. Some illustrative historical examples are given to highlight significant advances and capabilities in three areas of airborne measurement, ground-based measurements, and laboratory experiments, with a focus on cloud studies. The challenges of operating an aircraft and the inherent sampling limitation of high-speed nature and thus low spatial resolution of most measurement platforms are highlighted, and two developments are introduced to address these challenges: the emergence of uncrewed aerial vehicles (drones) for scientific purposes and the HOLODEC instrument based on digital in-line holography. The HOLODEC provides an estimate of the cloud particle size distribution and particle shape from a single sample volume of centimeter scales, providing unique opportunities to measure and study outstanding science questions such as droplet clustering, particle breakup, and particle shattering. It is pointed out that laboratory measurements have become somewhat less common and lagged field measurement capabilities, although their contributions have been profound.

The ultimate test of any models and thus parameterizations is its performance in climate simulations and weather prediction. Efficient and effective evaluation frameworks are needed to test the parameterizations, assess their predictive skills, characterize the model behavior from process level to global scale, and identify sources of potential errors to confidently guide further development. In Chapter 17, Lin and Xie describe the approaches and frameworks used for testing and evaluating fast physics parameterizations in climate and weather models. An integrated yet complementary modeling and evaluation framework is advocated that promotes process-oriented evaluation and effectively bridging parameterization development with observations and modeling, with focus on two exemplary frameworks that have been widely adopted by the modeling centers and the research community. The first is the integrated SCM-CRM-LES framework that has been widely used since it was promoted in the early 1990s. This modeling framework allows for process studies with SCMs, CRMs, and LES models with the scale ranging from a few hundred kilometers to a few tens of meters. With all the models driven by the same large-scale forcing and initial and boundary conditions, this frame has proven useful to identify strengths and weaknesses of model parameterizations. The second framework is based on the idea of running climate models in "weather forecast mode with initial data from NWP analyses to take advantage of the facts that (1) the large-scale state of the atmosphere in the early periods of a forecast is realistic enough that errors may be ascribed to the parameterizations of the atmospheric physical processes; (2) the atmospheric physical processes (e.g., moist process) are often fast (~hours) and the large-scale state changes slowly (~days); and (3) there is a strong correspondence between the short-term and long-term systematic errors in climate models, particularly for those fields that are related to fast physics (e.g., clouds)." Further integration of the two evaluation frameworks to better capitalize on their respective advantages is also explored. The metrics and diagnostics designed for model evaluation are presented as well, including process-oriented diagnostics and metrics in support of process studies, providing more insights into model errors, and satellite/radar simulator packages that permit direct comparison of model outputs to sensor signals without complicated retrievals.

1.4. HOW TO APPROACH THE CONTENT IN THIS BOOK

The book is targeted at researchers and graduate students working on the relevant areas. Each chapter of this collective volume has its own objectives that are closely related to other chapters and can be read either separately as a stand-alone chapter with its own list of references or together with the other chapters with cross-references as needed.

This book serves a valuable addition to existing literature on fast physics parameterizations in large-scale atmospheric models, with several unique features. It should be better read together with Stensrud (2007), the special fast physics collection in *Journal of Geophysical Research: Atmospheres* (Liu, 2019; https://agupubs.onlinelibrary.wiley.com/doi/toc/10.1002/(ISSN)2169-8996.FASTPHYS1), and various topical review articles (e.g., Morrison et al. (2020) on parameterizations of cloud microphysical processes).

ACKNOWLEDGMENTS

The volume editors thank all the chapter authors for their valuable contributions to this book. Dr. Leo Donner deserves special recognition; he co-convened with the editors various sessions on related scientific topics at the AGU Fall Meetings and helped with the conception of this book. The editors' relevant research has been mainly supported by the US Department of Energy's Office of Science Biological and Environmental Research program as part of the Atmospheric Systems Research (ASR) program and Earth System Modeling (ESM) program, and the Office of Energy Efficiency and Renewable Energy (EERE) under Solar Energy Technologies Office (SETO) award number 33504. Brookhaven National Laboratory is operated by Battelle for the US Department of Energy under contract DE-Sc01112704.

REFERENCES

Charney, J. G., Arakawa, A., Baker, D., Bolin, B., Dickenson, R., Goody, R., et al. (1979). *Carbon Dioxide and Climate: A Scientific Assessment*. Washington, DC: Natl. Acad. Sci.

Cheng, A., Xu, K.-M., & Stevens, B. (2010). Effects of resolution on the simulation of boundary-layer clouds and the partition of kinetic energy to subgrid scales. *Journal of Advances in Modeling Earth Systems*, *2*(3). doi:10.3894/JAMES.2010.2.3

Grabowski, W. (2001). Coupling cloud processes with the large-scale dynamics using the Cloud-Resolving Convection Parameterization (CRCP). *Journal of the Atmospheric Sciences*, *58*, 978–997.

Gustafson, W. I., Vogelmann, A. M., Li, Z., Cheng, X., Dumas, K. K., Endo, S., et al. (2020). The Large-Eddy Simulation (LES) Atmospheric Radiation Measurement (ARM) Symbiotic Simulation and Observation (LASSO) activity for continental shallow convection. *Bulletin of the American Meteorological Society*, *101*, E462–E479. doi:10.1175/bams-d-19-0065.1

Jakob, C. (2010). Accelerating progress in global atmospheric model development through improved parameterizations: Challenges, opportunities, and strategies. *Bulletin of the American Meteorological Society*, *91*(7), 869–876. https://doi.org/10.1175/2009BAMS2898.1

Kessler, E. (1969). On the distribution and continuity of water substance in atmospheric 1966 circulation. *Meteorological Monographs*, No. 32. Amer. Meteor. Soc., 84 pp.

Liu, Y. (2019). Introduction to special section on fast physics in climate models: Parameterization, evaluation and observation. *Journal of Geophysical Research: Atmospheres*, *124*, 8631–8644. https://doi.org/10.1029/2019JD030422

Liu, Y., Yau, M.-K., Shima, S., Lu, C., & Chen, S. (2023). Parameterization and explicit modeling of cloud microphysics: Approaches, challenges, and future directions. *Advances in Atmospheric Sciences*, *40*, 747–790. https://doi.org/10.1007/s00376-022-2077-3

Lovejoy, S., & Schertzer, D. (2010). Towards a new synthesis for atmospheric dynamics: Space–time cascades. *Atmospheric Research*, *96*, 1–52, doi:10.1016/j.atmosres.2010.01.004

Meehl, G. A., Senior, C. A., Eyring, V., Flato, G., Lamarque, J.-F., Stouffer, R. J., et al. (2020). Context for interpreting equilibrium climate sensitivity and transient climate response from the CMIP6 Earth system models. *Science Advances*, *6*, eaba1981. https://doi.org/10.1126/sciadv.aba1981

Mironov, D. V., & Machulskaya, E. E. (2017). A turbulence kinetic energy scalar variance turbulence parameterization scheme (Technical Report 575 No. 30). Consortium for Small-Scale Modeling. (http://www.cosmo576 model.org/content/model/documentation/techReports/docs/techReport 30.pdf)

Morrison, H., van Lier-Walqui, M., Fridlind, A. M., Grabowski, W. W., Harrington, J. Y., Hoose, C., et al. (2020). Confronting the challenge of modeling cloud and precipitation microphysics. *Journal of Advances in Modeling Earth Systems*, *12*, e2019MS001689. https://doi.org/10.1029/2019MS001689

Mülmenstädt, J., C. Nam, M. Salzmann, J. Kretzschmar, T. S. L'Ecuyer, U. Lohmann, P.-L., et al. (2020). Reducing the aerosol forcing uncertainty using observational constraints on warm rain processes. *Science Advances*, *6*, eaaz6433.

Parishani, H., M. Pritchard, C. Bretherton, M. Wyant, & M. Khairoutdinov (2017). Toward low-cloud permitting cloud superparameterization with explicit boundary layer turbulence. *Journal of Advances in Modeling Earth Systems*, *9*, 1542–1571. doi: 10.1002/2017MS000968

Rasch, P. J., Xie, S., Ma, P.-L., Lin, W., Wang, H., Tang, Q., et al. (2019). An overview of the atmospheric component of the Energy Exascale Earth System Model. *Journal of Advances in Modeling Earth Systems*, *11*, 2377–2411. doi: https://doi.org/10.1029/2019MS001629

Randall, D. (2013). Beyond deadlock. *Geophysical Research Letters*, *40*, 5970–5976. doi: 10.1002/2013GL057998

Stensrud, D. J. (2007). *Parameterization schemes. Keys to understanding numerical weather prediction models* (459 pp.). Cambridge: Cambridge University Press.

Stevens, B., Satoh, M., Auger, L., Biercamp, J., Bretherton, C. S., Chen, X., et al. (2019). DYAMOND: The Dynamics of the Atmospheric general circulation Modeled On Non-hydrostatic Domains. *Progress in Earth and Planetary Sciences*, *6*, 61. https://doi.org/10.1186/s40645-019-0304-z

Zelinka, M. D., Myers, T. A., McCoy, D. T., Po-Chedley, S., Caldwell, P. M., Ceppi, P., et al. (2020). Causes of higher climate sensitivity in CMIP6 models. *Geophysical Research Letters*, *47*, e2019GL085782. https://doi.org/10.1029/2019GL085782

Part I
Processes and Parameterizations

2

Radiative Transfer and Atmospheric Interactions

Yu Gu and Kuo-Nan Liou†

ABSTRACT

This chapter aims to provide a concise and comprehensive overview of the fundamental principles underlying radiative transfer processes and their interactions with the atmosphere. It encompasses discussions necessary for understanding radiative transfer parameterizations employed in modern climate models. Key concepts covered include emission, absorption, scattering, and the resolution of radiative transfer equations. Specifically, our focus is on the fundamentals of radiative transfer in the plane-parallel atmosphere. We thoroughly examine the intricate interactions between radiation and the Earth's atmosphere, including gaseous absorption and cloud-radiation interaction. The interaction between aerosols and radiation, on the other hand, is discussed in Chapter 3. Furthermore, we delve into the realm of three-dimensional (3D) radiative transfer, exploring its applications to understanding radiative processes in 3D clouds and mountainous regions. Additionally, we provide a brief review of commonly employed radiative transfer schemes in climate and weather research, using the Weather Research and Forecasting (WRF) model as an example.

2.1. BACKGROUND AND INTRODUCTION

Radiative transfer is a subject of study in a variety of fields, including astrophysics, applied physics, optics, planetary sciences, atmospheric sciences, meteorology, and various engineering disciplines. Prior to 1950, radiative transfer was studied principally by astrophysicists, although it was also an important research area in nuclear engineering and applied physics associated with neutron transport. In his groundbreaking book, Chandrasekhar (1950) presented the subject of radiative transfer in plane-parallel (PP; one-dimensional) atmospheres as a branch of mathematical physics and developed numerous solution methods and techniques. The field of atmospheric radiation, which evolved from the study of radiative transfer, is now concerned with the study, understanding, and quantitative analysis of the interactions of solar and terrestrial radiation with molecules, aerosols, and cloud particles in planetary atmospheres as well as the surface on the basis of the theories of radiative transfer and radiometric observations made from the ground, the air, and space (Liou, 1980, 2002). A fundamental understanding of radiative transfer processes is the key to understanding the atmospheric greenhouse effects and global warming, which results from external radiative perturbations of the greenhouse gases and air pollution, and to the development of methods to infer atmospheric and surface parameters through remote sensing.

Almost all the energy that drives the Earth's atmosphere and ocean currents originates from the Sun (Liou, 1992). Therefore, climate of the earth-atmosphere system is mainly determined by the radiation balance at the top of the atmosphere and the surface since radiation is the only

Joint Institute for Regional Earth System Science and Engineering, and Department of Atmospheric and Oceanic Sciences, University of California Los Angeles, Los Angeles, CA, USA

Fast Processes in Large-Scale Atmospheric Models: Progress, Challenges, and Opportunities, Geophysical Monograph 282, First Edition.
Edited by Yangang Liu and Pavlos Kollias.

DOI: 10.1002/9781119529019.ch02

mechanism by which the earth-atmosphere system gains or loses energy. The total radiant energy from the Sun varies only slightly, so we define a term solar constant or total solar irradiance (TSI) to represent the solar energy received per unit time and unit area at the top of the atmosphere when the Sun is at its mean distance from the Earth. On average, the TSI is 1361 W m^{-2} (Coddington et al., 2016) based on NASA's Solar Radiation and Climate Experiment (SORCE) (Rottman, 2005) Total Irradiance Monitor TIM (Kopp et al., 2005) measurements of total solar irradiance (Kopp & Lean, 2011). The Earth's atmosphere contains molecules, gases, aerosols, and clouds, which are significant components that are pertinent to the radiation and atmospheric interactions and determine the energy budget of the earth-atmosphere system. Figure 2.1 provides an updated estimation of the Earth's annual and global mean energy balance for the approximate period 2000–2010 (Stephens et al., 2012). The incoming solar flux for climatological energy balance is about 340 W m^{-2} (round off the decimal point). About 23% of the incoming solar radiation gets reflected by clouds, aerosols, and atmospheric gases and 7% is reflected by surface, providing a planetary albedo of about 30%. About 22% of the incoming solar flux is absorbed by the atmosphere while another half is absorbed by the Earth's surface, resulting from the divergence of net solar fluxes at the top of the atmosphere and the surface. The solar fluxes absorbed by the surface are transferred to the atmosphere by means of the convection and conduction of sensible heat from the surface, by the latent heat of condensation released in precipitation processes, as well as by emission of longwave or thermal infrared (IR) radiation. The global/annual mean upwelling longwave flux of 398 W m^{-2} is equivalent to an effective emission temperature of 289 K. This surface thermal IR radiation is largely absorbed by clouds, aerosols, and greenhouse gases. The atmosphere in turn radiates longwave fluxes downward back to Earth and upward to space. At the top of the atmosphere, the energy is balanced by radiative flux exchanges. At the surface, however, upward sensible and latent heat fluxes must be introduced to maintain radiative flux balance.

The above energy balance of the earth-atmosphere system is obtained when we treat the entire Earth as a single point. Earth's climate is determined by the flows of energy into and out of the planet, and changes to the surface energy balance ultimately also control how the hydrological cycle responds to the small energy imbalances that force climate change. Geographical distributions of these energy flows in the earth-atmosphere system are also particularly important as they drive ocean circulations, fuel the evaporation of water from the Earth's surface, and govern the planetary hydrological cycle (Stephens et al., 2012). Radiative transfer schemes have been used in climate models to compute radiative fluxes and heating rates over regional and global scales in the earth-atmosphere system. In this chapter, we present the fundamentals of radiative transfer in the plane-parallel atmosphere, the interactions between radiation and the Earth's atmosphere (including gaseous absorption and cloud-radiation interaction; aerosol-radiation interaction is covered in Chapter 3), three-dimensional (3D) radiative transfer for 3D clouds and over the mountainous regions,

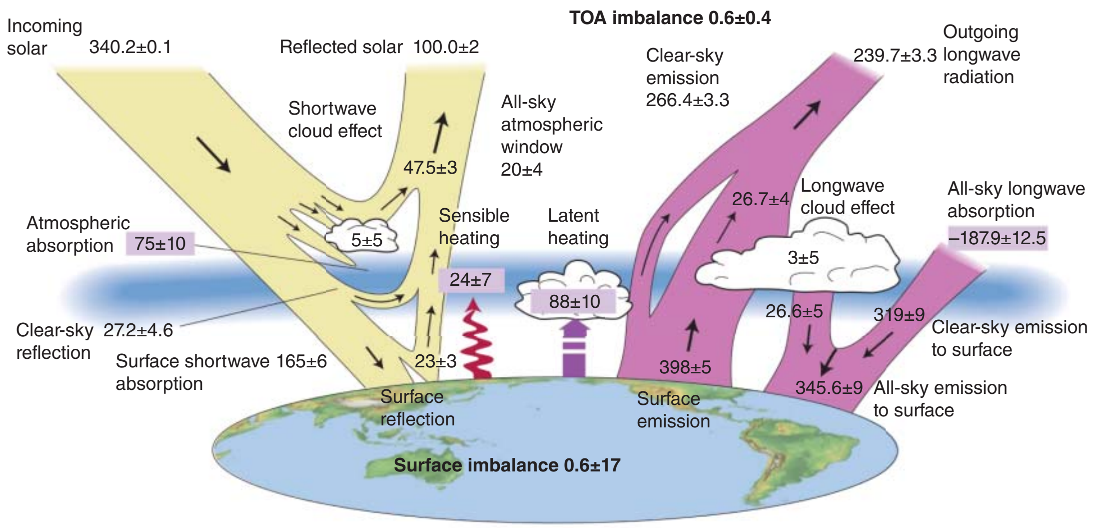

Figure 2.1 Estimate of the Earth's annual and global mean energy balance for the approximate period 2000–2010. Source: Stephens et al. (2012)/Springer Nature.

and a brief review of the commonly used radiative transfer schemes in the climate and weather research using the Weather Research and Forecasting (WRF) model as an example.

2.2. FUNDAMENTALS AND EQUATION GOVERNING RADIATIVE TRANSFER FOR PLANE-PARALLEL ATMOSPHERE

In radiation, we use the Planck function to relate the emitted radiation intensity to the wavelength and the temperature of the emitting substance:

$$B_\lambda(T) = \frac{2hc^2}{\lambda^5(e^{hc/K\lambda T} - 1)}, \tag{2.1}$$

where h is the Planck's constant, λ is the wavelength, K is Boltzmann's constant, c is the velocity of light, and T is the absolute temperature. Figure 2.2 illustrates the curves of the intensity as a function of wavelength for a star with a temperature range similar to the Sun (~6000 K, on the left) and a planet similar to the Earth (~288 K, on the right). Two facts are evident from the figures and also can be derived from the Planck function: first, the intensity of emitted radiation increases with temperature. The intensity from the Sun is much larger than that from the Earth since the Sun has a much higher temperature. Second, the wavelength of the maximum intensity decreases with increasing temperature, which can be seen from the shift of the location of the maximum values from right (longer wavelengths) to the left (shorter wavelengths) as temperature increases. For the Sun, the maximum intensity is located at about 0.5 μm, while for the Earth, it is located at about 12 μm.

When a beam of light travels through the atmosphere, the energy it carries will be weakened by its interaction with the matter in the atmosphere, such as molecules, gases, cloud particles, and aerosols. Two major processes are considered in the radiative transfer. One is extinction and the other is the source or contribution. Extinction consists of two distinct processes, scattering and absorption. Figure 2.3 illustrates how the particles in the atmosphere scatter and absorb sunlight. Depending on the size and single-scattering properties of the particles, when a beam of sunlight hit on a particle, some energy gets absorbed and transformed to heat. Some light gets scattered and the energy is redirected to different directions. The extinction of light is determined by the so-called extinction coefficient or extinction cross section $k(\nu)$, where ν represents a certain wavenumber. There are two types of scattering: Rayleigh scattering occurs when the particle size is much smaller than the wavelength. This normally happens for molecules in the atmosphere, and the scattered intensity is inversely dependent on the wavelength to the fourth power. Lorenz-Mie scattering is for spherical particles with sizes comparable to or larger than the wavelength, such as aerosols and cloud droplets. The Mie theory is basically a solution to Maxwell's equation that takes the form of analytical infinite series.

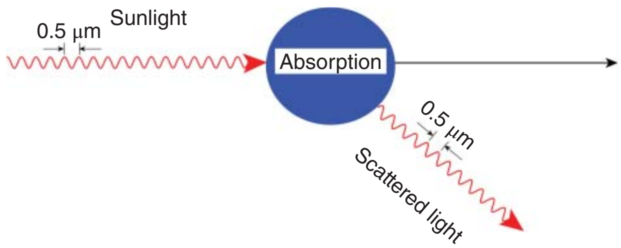

Figure 2.3 Diagram illustrating the scattering and absorption of sunlight by a particle in the atmosphere.

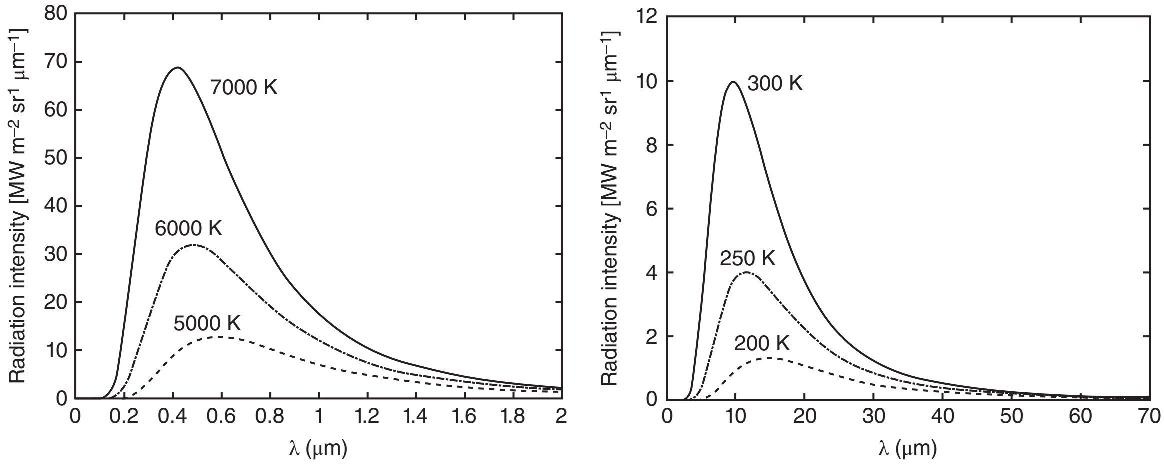

Figure 2.2 The radiation intensity as a function of wavelength for the Sun (~6000 K, left) and the Earth (~300 K, right). Also shown are the curves for a few other temperatures.

On the other hand, the radiation intensity may be strengthened by emission from the materials and scattering from all other directions. We define a source function coefficient j_v to describe the emission and scattering process. Combining the extinction and source processes, we obtain the basic radiative transfer equation in the form shown below for a given wavenumber v:

$$dI_v = -k(v) I_v \rho_a ds + j_v \rho_a ds, \tag{2.2}$$

where I_v is the radiation intensity which is a function of solid angle, $k(v)$ is the mass absorption coefficient with units of $m^2\ kg^{-1}$, and ρ_a is the air density. For source or contribution, three factors are considered: (1) emission by the matter, such as from clouds; (2) single scattering of direct solar flux which is associated with the exponential attenuation to the level τ based on extinction law; and (3) the multiple scattering. We further introduce two parameters to represent single scattering and multiple scattering: one is phase function or asymmetry factor, which represents the angular distribution of scattered energy as a function of direction; the other one is single-scattering albedo, defined as the ratio of the scattering cross section to the total extinction (scattering plus absorption) cross section. So, the fundamental parameters in radiative transfer, also called single-scattering properties, are extinction coefficient, single-scattering albedo, and phase function or asymmetry factor. These parameters are functions of the incident wavelength, particle size and shape, and refractive index with respect to wavelength. The refractive index consists of a real part and an imaginary part, corresponding to the scattering and absorption properties, respectively.

In radiative transfer, it is commonly assumed that the atmosphere in a local position is plane-parallel, that is, variations in the radiation intensity and atmospheric parameters, such as temperature and gaseous profiles, are permitted only in the vertical direction. So, changes in distance can be expressed in terms of changes in height together with the cosine of the solar zenith angle μ. The solar zenith angle θ is defined to be the angle between the center of the Sun's disc and the zenith (a line that goes straight up directly above a particular location; Fig. 2.4). Normally, we are interested in the total extinction over a finite distance and hence define a physical parameter called optical depth τ, which is the integration of extinction coefficient over the depth of an atmospheric layer:

$$\tau(v) = \int_z^{z_\infty} k_v(z')\rho_a(z')dz', \tag{2.3}$$

so that $d\tau = -k_v \rho_a dz$. Then, we obtain the fundamental equation governing the transfer of diffuse solar radiation for the problem of multiple scattering in plane-parallel atmospheres in terms of τ, μ, and azimuthal angle in reference to the x-axis ϕ and by measuring intensity downward from the outer boundary (top of the atmosphere):

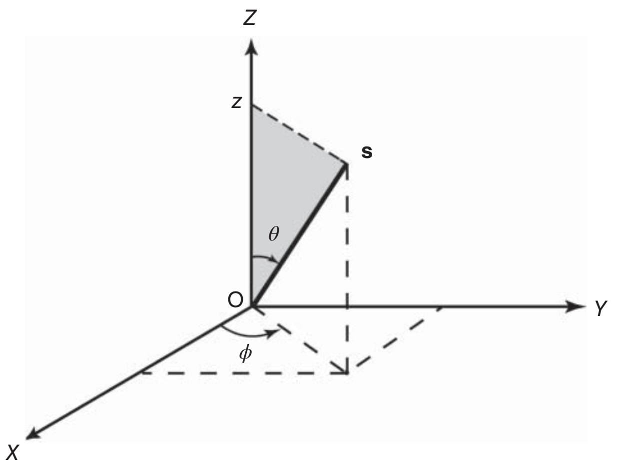

Figure 2.4 Definitions of the zenith angle θ and the azimuthal angle ϕ with reference to the Cartesian coordinate system (x, y, z), where s represents a position vector in space.

$$\mu \frac{dI(\tau,\mu,\phi)}{d\tau} = I(\tau,\mu,\phi) - J(\tau,\mu,\phi). \tag{2.4}$$

The solar azimuth angle ϕ is the angular distance measured in terms of a 360-degree compass between the x-axis and the projection of the line of sight to the Sun on the ground (Fig. 2.4). Here, we ignore the subscript representing the wavenumber or wavelength, and $J(\tau, \mu, \phi)$ is the source function.

Diffuse solar radiation is associated with multiple scattering processes and is differentiated from direct solar radiation. Considering a vertical layer, the differential change of disuse solar radiation after passing through the layer is due to the following processes: (1) reduction from the extinction attenuation, (2) increase from the single scattering of the unscattered direct solar flux from the original incident direction ($-\mu_0$, ϕ_0) to (μ, ϕ), (3) increase from multiple scattering of the diffuse intensity from directions (μ', ϕ') to (μ, ϕ), and (4) increase from emission within the layer in the direction (μ, ϕ) under the Kirchhoff's law referring to wavelength-specific radiative emission and absorption by a material body in thermal equilibrium condition. Let the phase function corresponding to a volume of particulates be P and $P(\mu, \phi; \mu', \phi')$ denotes the redirection of the incoming intensity defined by (μ', ϕ') to the outgoing intensity defined by (μ, ϕ). The source function $J(\tau, \mu, \phi)$ is then given by

$$\begin{aligned} J(\tau,\mu,\phi) = {} & \frac{\varpi}{4\pi}\int_0^{2\pi}\int_{-1}^{1} I(\tau,\mu',\phi')P(\mu,\phi;\mu',\phi')d\mu' d\phi' \\ & + \frac{\varpi}{4\pi}F_\odot P(\mu,\phi;-\mu_0,\phi_0)e^{-\tau/\mu_0} \\ & + (1-\varpi)B[T(\tau)], \end{aligned} \tag{2.5}$$

where $F_{\odot}$ is the incident solar radiation at the top of the atmosphere, ϖ is the single-scattering albedo, and the first, second, and third terms on the right-hand side represents contributions from multiple scattering, single scattering, and emission, respectively.

2.3. GASEOUS ABSORPTION

To describe the interactions of radiation with the Earth's atmosphere, we must understand the atmosphere's composition and structure. The atmosphere is composed of two types of gases, one with nearly permanent concentrations and another with variable concentrations. The atmosphere also contains aerosols, clouds, and precipitation that are highly variable in space and time. The most abundant gas in the atmosphere is nitrogen (~78%), followed by oxygen (~21%) and argon (~1%), which account for more than 99.96% of the atmosphere by volume. The concentrations of these gases, referred to as permanent constituents, are well mixed in the atmosphere with nearly constant volume ratios up to about 60 km in altitude. The amounts of variable gases vary significantly with both space and time and are extremely important in the radiation budget of the atmosphere although they are small. There are a number of trace gases, such as carbon dioxide (CO_2), nitrous oxide (N_2O), methane (CH_4), ozone (O_3), chlorofluorocarbons (CFCs), nitrogen oxides (NO_x), Sulfur oxides (SO_x), and volatile organic carbons (VOCs), which absorb and emit infrared radiation. These are called greenhouse gases and play an essential role in the Earth's energy budget. Besides the trace gases, water vapor is also a major radiative, dynamic, and thermodynamic element in the atmosphere with highly variable mixing ratio. Water vapor is known to be Earth's most abundant greenhouse gas through feedback (Liou, 2002). Increased greenhouse gases in the atmosphere makes the atmosphere more humid, and the increase in humidity amplifies the warming from carbon dioxide. Human activities are most likely to affect the trace gases rather than the permanent gases such as nitrogen and oxygen (Liou, 2002). Among them, carbon dioxide (CO_2) is the most important anthropogenic greenhouse gas with a concentration of ~400 ppm (parts per million in volume) in 2014 and ~407 ppm in 2018, increasing by about 0.4% per year as a result of the combustion of fossil fuels, absorption and release by the oceans, and photosynthesis. Another important variable gas is ozone, which occurs at altitudes between 15 and 30 km with a maximum concentration at ~20–25 km depending on latitude and season. The absorption of solar ultraviolet (UV) radiation by the ozone layer is essential to life on the Earth. Ozone can also be formed in the troposphere by the interaction of ultraviolet light with hydrocarbons and nitrogen oxides, which are emitted by automobile tailpipes and smokestacks. Tropospheric ozone is considered as both air pollutants and greenhouse gases. Nitrogen oxides emitted by transportation and combustion processes at the surface and by aircraft in the upper troposphere and lower stratosphere are important in the determination of ozone concentrations. For methane, a number of measurements indicate that its concentration has increased by 1%–2% per year. The most likely cause is the greater biogenic emissions associated with an increasing human population. There is also some evidence of an increase in N_2O of about 0.2% per year, attributed to the combustion of fossil fuels and, in part, to fertilizer denitrification.

The Earth's atmosphere is divided into different layers—troposphere, stratosphere, mesosphere, and thermosphere—based on vertical temperature profile. The troposphere is characterized by a decrease in temperature with respect to height, up to about 12 km, with a global mean lapse rate of about 6.5 K km^{-1}. The temperature profile in this layer is a result of the radiative balance and transport of energy from surface to the atmosphere. About 80% of the atmosphere is concentrated in this layer, with almost all water vapor, clouds, and precipitation confined below the tropopause—the top of the troposphere. The stratosphere represents an isothermal layer from the tropopause to about 20 km, followed by a layer with increasing temperature with altitude at an average rate of 5 K km^{-1}, largely due to the absorption of Sun's ultraviolet radiation by ozone. The water vapor in the troposphere does not mix much with that above the tropopause due to the temperature inversion in the stratosphere. The temperature in the mesosphere decreases again with altitude from about 50 to 80 km. The air is well mixed from the ground to the top of the mesosphere with composition of gases almost identical except for water vapor and ozone. The thermosphere is the region above the top of mesosphere where the temperature begins to rise again to as high as 2000 K, associated with the absorption of solar radiation by atomic oxygen. This is because the atmosphere there is very thin, so a little heating can significantly raise the temperature.

Figure 2.5 illustrates the results calculated by LINEPAK (Gordley et al., 1994) using the HITRAN2004 (Rothman et al., 2005) spectroscopic database assuming the U.S. 1976 Standard Atmosphere and the solar zenith angle of 0° (Liou & Yang, 2016). The upper panel of Figure 2.5 illustrates solar and thermal IR spectral irradiances at the top of the atmosphere as a function of wavelength and wavenumber. The solar and thermal IR spectra cover wavelength ranges from ~0.1 to 5 and ~5 to 100 μm, respectively, with a slight overlap between ~3 and 5 μm. The middle panel shows absorption by various gases and Rayleigh scattering. The bottom panel illustrates the total atmospheric absorption in terms of the percentage

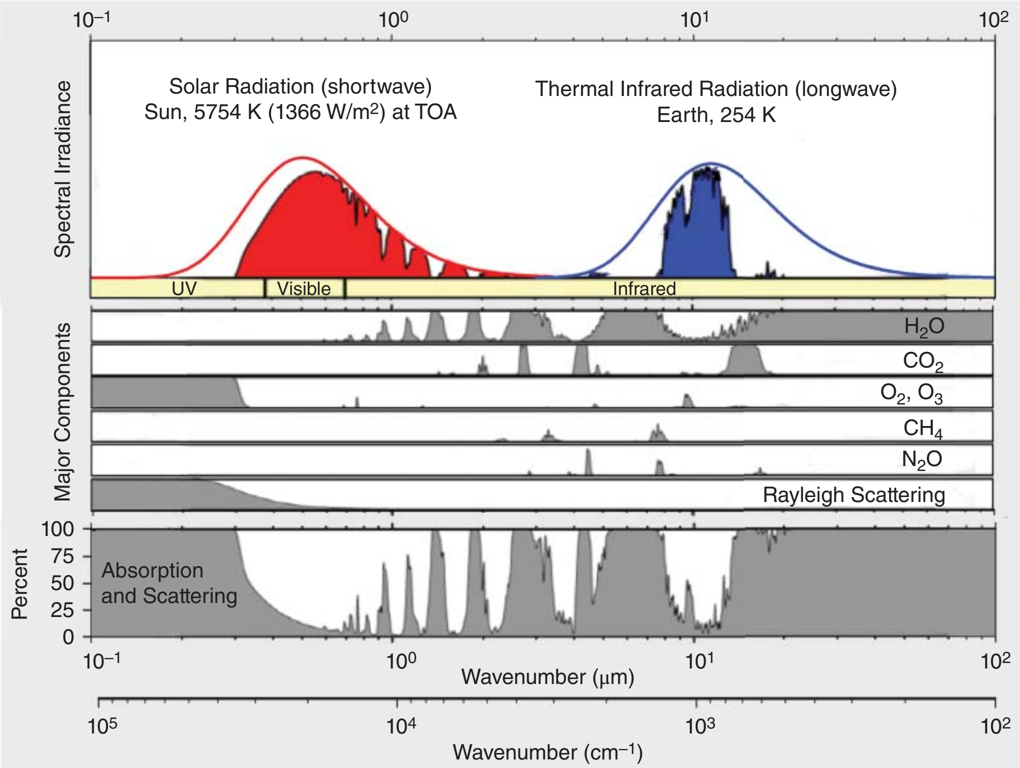

Figure 2.5 Top panel: Spectral irradiances for the solar (red curve) and thermal IR (blue curve, scaled with reference to solar) regions as a function of wavelength and wavenumber. The red area denotes the observed solar fluxes available at the surface; the blue area represents the thermal IR fluxes absorbed in the atmosphere and available at the top of the atmosphere. Middle panel: Absorption by H_2O, CO_2, O_2, O_3, CH_4, and N_2O, and Rayleigh scattering. Bottom panel: Total atmospheric absorption in terms of the percentage of the entire atmosphere corresponding to the U.S. 1976 Standard Atmosphere; 0% and 100% indicate that the atmosphere is clear (total transmission) and opaque to radiation, respectively.

of the entire atmosphere corresponding to the U.S. 1976 Standard Atmosphere.

2.3.1. Absorption in Solar Spectra

The solar spectrum (red curve) is computed from Planck emission at the Sun's photosphere temperature of 5754 K and attenuated to the top of the atmosphere coupled with a corresponding solar constant of 1366 W m^{-2}. The observed solar fluxes available at the surface is represented by the red area (top panel of Fig. 2.5). The depletion of solar flux in the UV region with wavelength shorter than 0.4 μm is mainly due to the absorption of molecular oxygen and ozone together with Rayleigh scattering (middle panel of Fig. 2.5). In the visible region (between 0.4 and 0.7 μm), the depletion is caused by the absorption produced by oxygen, ozone (O_3), and water vapor (H_2O), but main attenuation is associated with Rayleigh scattering. Absorption lines by H_2O produced by vibration-rotation transitions are located at 0.72, 0.82, 0.94, 1.1, 1.38, 1.87, 2.7, and 3.2 μm. In the near thermal IR, the primer absorber is water vapor and carbon dioxide. Absorption due to CO_2 is largely produced by vibrational transitions with spectral bands located at 1.6, 2.0, 2.7, and 4.3 μm in the solar spectrum. H_2O rational lines essentially cover the entire solar spectra. Other minor absorbers in the solar spectra include N_2O (nitrous oxide) and CH_4 (methane).

The bottom panel of Figure 2.5 illustrates the total atmospheric absorption produced by the various molecules discussed above in terms of the percentage of the entire atmosphere corresponding to the U.S. 1976 Standard Atmosphere. Here, 0% and 100% indicate that the gas is clear (total transmission without absorption) and opaque to radiation, respectively. This information is essential to the development of space remote sensing of the atmosphere, oceans, and land surfaces, employing UV, visible, and thermal IR techniques. Note that Rayleigh scattering occurs primarily in the UV and visible regions.

2.3.2. Absorption in Thermal Infrared Spectra

The thermal IR spectrum (blue curve in the top panel of Fig. 2.5) is computed from the global equilibrium temperature of the earth-atmosphere system of 254 K, and its peak is normalized with reference to the solar spectral peak. The blue area denotes the thermal IR fluxes absorbed in the atmosphere and available at the top of the atmosphere. A few important bands include carbon dioxide (CO_2) 4.3 and 15 μm bands, O_3 9.6 μm band, H_2O 6.25 μm band, and 10 μm continuum band in the thermal IR window. The middle panel of Figure 2.5 shows absorption by H_2O produced by vibration-rotation transitions located at 6.3 μm in the thermal IR spectrum. Similar to that in the solar spectra, H_2O rational lines cover the entire thermal IR spectra, but these absorption lines are strongest at wavelengths longer than ~12 μm, known as the rotational band of water vapor. The strong CO_2 15 μm band in the thermal IR spectrum is most pronounced in trapping the emission from the surface and lower atmospheres. This band is the source of about half of the radiative forcing due to anthropogenic greenhouse warming since the era of the Industrial Revolution. Other minor absorbers in the thermal IR spectra include methane (CH_4), N_2O, and CFCs.

Greenhouse gases are those that absorb and emit infrared radiation in the wavelength range emitted by the Earth. The most important greenhouse gases in the Earth's atmosphere include H_2O, CO_2, CH_4, N_2O, O_3, CFCs, and hydrofluorocarbons (including HCFCs and HFCs). These gases mostly transmit visible radiation and partially absorb infrared radiation (between about 4 and 30 μm wavelength) and hence play an important role in the energy budget of the earth-atmosphere system by trapping the IR radiation and warming the Earth's surface temperature by about 33 K.

2.3.3. Absorption Coefficient

The emission spectra of certain gases are composed of a large number of individual spectral lines. However, monochromatic emission is practically never observed. Radiation emitted during repeated energy transitions is non-monochromatic, and spectral lines of finite widths are observed. The broadening of lines is mainly caused by collision, referred to as pressure broadening, and the Doppler effect resulting from the difference in thermal velocities of atoms and molecules.

Absorption line parameters for various gases can be computed from fundamental quantum mechanics theory or measured through lab experiments. Based on theory and measurements, line parameters have been compiled over the range 0–17,900 cm^{-2} (Rothman et al., 1998) with data for more than 1 million lines. The strength of absorption is normally represented by the absorption coefficient that is a function of wavenumber, pressure, and temperature, and can be written in the form

$$k(\nu, p, T) = \sum_{i=1}^{N} S_i(T) f_{\nu,i}(\nu, p, T), \tag{2.6}$$

where S_i is the line strength for the ith absorption line and $f_{\nu,i}$ is the line shape.

Ideally, the absorption coefficients should be computed at wavenumbers, temperatures, and pressures, which are as closely spaced as possible. However, due to computing resource limitations, these spacings would be chosen as large as possible while still retaining the high degree of accuracy needed for climate studies. Here, an example of computing the absorption coefficients for any pressures and temperatures is provided. The absorption coefficients for a given wavenumber and particular gas can be parameterized as a function of pressure and temperature according to Chou and Kouvaris (1986) in the following form:

$$\ln k(\nu, p, T) = \sum_{n=0}^{2} a_n(\nu, p)(T - 250)^n. \tag{2.7}$$

For a given wavenumber and pressure, three temperatures (e.g., 200, 250, and 300 K) can be used to determine the coefficients that can be tabulated at various prescribed pressures for the solar and thermal infrared calculations. The absorption coefficients at other pressures can be linearly interpolated in the pressure coordinate (Fu & Liou, 1992).

2.3.4. Absorption Integration Methods

For solar radiation, if we consider a nonscattering atmosphere and a small spectral interval $\Delta\nu$ such that the spectral solar flux can be taken as constant, the downward solar flux at a given level z can be written in the form

$$F_\nu^{\downarrow}(z) = \mu_0 T_\nu(z/\mu_0) S_\nu \Delta\nu, \tag{2.8}$$

where $S\Delta\nu$ represents the incident solar flux, μ_0 is the cosine of the solar zenith angle, and T_ν is the spectral-mean transmittance over the spectral interval $\Delta\nu$ defined by

$$T_\nu(z/\mu_0) = \int_{\Delta\nu} \exp\left[-\int_z^{\infty} k(\nu, p, T)\rho_a/\mu_0 \mathrm{d}z'\right] \frac{\mathrm{d}\nu}{\Delta\nu}, \tag{2.9}$$

where ρ_a denotes the density of the absorbing gas.

For thermal infrared radiation, similarly, the spectral-mean transmittance between levels z and z' is given by

$$T_\nu(z, z'; \mu) = \int_{\Delta\nu} \exp\left[-\int_z^{z'} k(\nu, p, T)\rho_a/\mu \mathrm{d}z''\right] \frac{\mathrm{d}\nu}{\Delta\nu}. \tag{2.10}$$

Transmittance computation can be performed by a line-by-line (LBL) technique or simplified approaches such as the correlated k-distribution (CKD) method.

For a given wavenumber and species, contributions to transmittance arise from the absorption coefficients for N lines as shown in equation (2.6). In order to resolve individual lines in the LBL approach, the absorption coefficient must be computed as wavenumber intervals that are smaller than the line half-width. In the troposphere, absorption due to H_2O generally dominates; however, there are also a number of absorption bands associated with CO_2. Absorption due to CO_2 at the 15 μm vibration and rotation bands is critically important concerning greenhouse warming. H_2O lines are broadened by collision, and their half-widths are $>0.01\,\mathrm{cm}^{-1}$. Therefore, computations must be performed at about 1 million points to resolve H_2O lines. In the stratosphere, absorption and emission processes are dominated by CO_2 and O_3. Broadening of the absorption lines is mainly due to the Doppler effect with a half-width of about 0.0005–$0.001\,\mathrm{cm}^{-1}$. The computations must be performed at more than half a million points if individual lines are to be resolved. Furthermore, for each point, there are numerous lines and atmospheric conditions that must be considered for applications to atmospheric radiative transfer. The computer time required for line-by-line calculations is very expensive, especially for flux calculations in which an integration over all absorption bands is necessary.

The k-distribution method is based on the grouping of gaseous spectral transmittance according to the absorption coefficient k. Under a homogeneous condition where pressure and temperature are constant, for a given absorption gas and spectral interval $\Delta\nu$, we may introduce the k-distribution function $h(k)$, which is the probability density function such that $h(k)\mathrm{d}k$ is the fraction of $\Delta\nu$ within which the absorption coefficient is between k and $k + \mathrm{d}k$. The spectral-mean transmittance should be dependent on the k-distribution but independent of the ordering of k (Arking & Grossman, 1972). Hence, we may replace the wavenumber integration by an integration over k space. The spectral-mean transmittance may be expressed by

$$T_\nu(u) = \int_{\Delta\nu} \mathrm{e}^{-k(\nu)u}\frac{\mathrm{d}\nu}{\Delta\upsilon} = \int_0^\infty \mathrm{e}^{-ku}h(k)\mathrm{d}k, \qquad (2.11)$$

where $u(z) = \int_z^{z_\infty} \rho_a(z')\mathrm{d}z'$ is the path length (g cm^{-2}) to denote the amount of absorber, and $h(k)$ is normalized to 1 in the domain $(0, \infty)$. This equation defines the k-distribution method for the homogeneous atmosphere.

We may further define a monotonically increasing and smooth cumulative probability function in k space in the form

$$\mathrm{g}(k) = \int_0^k h(k)\mathrm{d}k, \qquad (2.12)$$

where $g(0) = 0$, $g(k\to\infty) = 1$, and $\mathrm{d}g(k) = f(k)\mathrm{d}k$. The spectral-mean transmittance can then be expressed in terms of cumulative probability g as

$$T_\nu(u) = \int_{\Delta\nu} \mathrm{e}^{-k(\nu)u}\frac{\mathrm{d}\nu}{\Delta\upsilon} = \int_0^1 \mathrm{e}^{-k(\mathrm{g})u}\mathrm{dg} \cong \sum_{i=1}^{M} \mathrm{e}^{-k(\mathrm{g}_i)u}\Delta\mathrm{g}_i, \qquad (2.13)$$

where $k(g)$ is the inverse function of $g(k)$ and must also be a smooth function in g space. Here, the integration in g space replaces the tedious wavenumber integration and can be evaluated by a finite sum of exponential terms as shown in equation (2.13).

The k-distribution method can be further extended to nonhomogeneous atmosphere, referred to as the correlated k-distribution method. In this method, the vertical nonhomogeneity of the atmosphere is accounted for by assuming a simple correlation of k-distribution at different temperatures and pressures. The CKD approach allows the use of k-distribution method at each altitude and can be used for absorption bands in both solar and thermal infrared spectra. Proof of the validity of CKD and its accuracy under various atmospheric conditions have been carried out by a number of studies (e.g., Fu & Liou, 1992; Goody et al., 1989). Errors in flux calculations associated with CKD with respects to LBL results are generally on the order of 1%. At the same time, the results from CKD can be directly incorporated into multiple scattering processes associated with cloud and aerosol processes. Thus, the CKD method is a powerful technique in the parameterization of radiative transfer in climate models where cloud and aerosol processes must be accounted for in flux and heating rate calculations.

Domoto (1974) and Wang and Ryan (1983) illustrated the importance of treating overlap absorption in radiative transfer calculations and climate studies. Goody et al. (1989), Lacis and Oinas (1991), Fu and Liou (1992), and Shi (1998) pointed out that overlap absorption by several different gases is an important theoretical and practical problem in CKD since computational speed is essential to radiative transfer modeling, especially when it is applied to the scattering atmosphere. Lacis and Oinas (1991) adopted the multiplication rule for transmittance computations under which the absorption spectra for two gases are assumed to be uncorrelated. Mlawer et al. (1997) developed a method to treat bands containing gases with overlap absorption, in which the key absorbers in each spectral band are treated with high accuracy, whereas a less detailed procedure is employed to compute absorption due to minor gases in the band.

In Fu and Liou (1992), two different approaches were employed to treat overlap absorption in the g space. These approaches have been proven to be both efficient and accurate for treating the overlap problem involving atmospheric radiative transfer. The first approach uses the multiplication assumption in which the absorption of different gases are assumed to be uncorrelated so that the total transmittance can be obtained by the product of the transmittance from each gas. Fu and Liou (1992) concluded that the multiplication approach for overlap gases can achieve excellent accuracy in flux and heating rate calculations over a spectral interval of about 150 cm^{-1}. In the second approach, a new absorption coefficient, which can be considered as the absorption coefficient for a single-mixture gas, is defined. The second approach does not require the assumption that the two absorption spectra are uncorrelated, and it is computationally more efficient.

2.4. COMMONLY USED APPROXIMATIONS OF RADIATIVE TRANSFER

In section 2.2, we introduce the basic radiative transfer equation for the plane-parallel condition (equation (2.5)). For calculations of solar fluxes in the atmosphere, the azimuthal dependence of the intensity expansion can be neglected and we may define the phase function as

$$P(\mu,\mu') = \frac{1}{2\pi}\int_0^{2\pi} P(\mu,\phi;\mu',\phi')\mathrm{d}\phi'. \tag{2.14}$$

The azimuthally independent transfer equation for diffuse radiation can be written as

$$\mu\frac{\mathrm{d}I(\tau,\mu)}{\mathrm{d}\tau} = I(\tau,\mu) - \frac{\varpi}{2}\int_{-1}^{1} I(\tau,\mu')P(\mu,\mu')\mathrm{d}\mu' - \frac{\varpi}{4\pi}F_\odot P(\mu,-\mu_0)\mathrm{e}^{-\tau/\mu_0} - (1-\varpi)B[T(\tau)]. \tag{2.15}$$

The above radiation equation is for radiance or intensity. In climate model applications, radiation fluxes are normally needed and can be obtained by the integration of radiation intensity over the hemisphere for upward and downward directions, respectively:

$$F^{\uparrow}_{\mathrm{dif}}(\tau) = \int_0^{2\pi}\int_0^{1} I(\tau,\mu,\phi)\mu\mathrm{d}\mu\mathrm{d}\phi = 2\pi\int_0^1 I(\tau,\mu)\mu\mathrm{d}\mu, \qquad \mu \geq 0, \tag{2.16}$$

$$F^{\downarrow}_{\mathrm{dif}}(\tau) = \int_0^{2\pi}\int_0^{-1} I(\tau,\mu,\phi)\mu\mathrm{d}\mu\mathrm{d}\phi = 2\pi\int_0^{-1} I(\tau,\mu)\mu\mathrm{d}\mu, \qquad \mu \leq 0, \tag{2.17}$$

Note that for thermal infrared radiation, the direct solar term involving $F_\odot$ (the third term on the right-hand side) does not appear. For solar radiation, the thermal infrared emission term (the fourth term on the right-hand side) will be omitted. In addition, the above equation only describes the diffuse component. We must include the direct component in the calculations of the downward solar radiation. This is given by the simple Beer-Bouguer-Lambert law that describes the extinction of solar radiation in the form

$$F^{\downarrow}_{\mathrm{dir}} = \mu_0 F_\odot \mathrm{e}^{-\tau/\mu_0}. \tag{2.18}$$

The total upward and downward flux densities at a given τ are

$$F^{\uparrow}(\tau) = F^{\uparrow}_{\mathrm{dif}}(\tau) = 2\pi\int_0^1 I(\tau,\mu)\mu\mathrm{d}\mu, \tag{2.19}$$

$$F^{\downarrow}(\tau) = F^{\downarrow}_{\mathrm{dif}}(\tau) + F^{\downarrow}_{\mathrm{dir}}(\tau) = 2\pi\int_0^{-1} I(\tau,\mu)\mu\mathrm{d}\mu + \mu_0 F_\odot \mathrm{e}^{-\tau/\mu_0}. \tag{2.20}$$

Thus, the net flux for a given level z is

$$F(z) = F^{\downarrow}(z) - F^{\uparrow}(z). \tag{2.21}$$

For an atmosphere layer with thickness of Δz, the radiative heating in the atmosphere is produced by the divergence of the net flux and is given by

$$\frac{\partial T}{\partial t} = -\frac{1}{\rho C_\mathrm{p}}\frac{\Delta F(z)}{\Delta z}, \tag{2.22}$$

where T is the temperature, ρ is air density, C_p is the specific heat at constant pressure, and $\Delta F(z) = F(z) - F(z+\Delta z)$.

There are quite a few methods available to provide exact solutions to the radiative transfer equation, including discrete-ordinates method, invariance method, and adding method. The discrete-ordinates method was first developed by Chandrasekhar (1950) and was proved by Liou (1973) to be a useful and powerful method for the computation of radiation in aerosol and cloudy atmospheres. The principle of the adding method was stated by Stokes (1862) when dealing with reflection and transmission by glass plates. van de Hulst (1980) presented a set of adding equations that is now commonly used for multiple scattering. Takano and Liou (1989) modified the adding method for application to randomly oriented ice crystals. The exact adding/doubling method appears to be a powerful tool for multiple scattering calculations, particularly for remote sensing applications from the ground, the air, and space. The discrete-ordinates and adding methods are similar in terms of numerical calculations. The invariance method is, in principle, equivalent to the adding method (Liou, 2002). In this chapter, we focus on the discrete-ordinates method and its approximations.

The discrete-ordinates method involves the discretization of the basic radiative transfer equation and the solution of a set of first-order differential equations.

In order to solve equation (2.15) analytically, the integral must be replaced by a summation over a finite number of quadrature points. The use of Gaussian quadrature is essential because it makes phase function renormalization unnecessary, implying that energy is conserved in the computation (Stamnes et al., 1988). In numerical integrations, double-Gauss's formula has been found to be superior to other formulas for quadratures in the interval $(-1, 1)$. Double-Gauss simply refers to a quadrature rule suggested by Sykes (1951) in which the Gaussian formula is applied separately to the half-ranges $-1 < \mu < 0$ and $0 < \mu < 1$. For any function $f(\mu)$, double-Gauss's formula is expressed by

$$\int_{-1}^{1} f(\mu)\mathrm{d}\mu \approx \sum_{j=-n}^{n} w_j f(\mu_j), \tag{2.23}$$

where the weights w_j are

$$w_j = \frac{1}{P'_{2n}(\mu_j)} \int_{-1}^{1} \frac{P_{2n}(\mu)}{\mu - \mu_j}\mathrm{d}\mu, \tag{2.24}$$

and μ_j are the zeros of the even-order Legendre polynomials $P_{2n}(\mu)$, and the prime denotes the differentiation with respect to μ_j. Also, the quadrature weights of w and discrete ordinate of μ can be selected to satisfy $w_{-j} = w_j$ ($\sum_{j=-n}^{n} w_j = 2$) and $\mu_{-j} = -\mu_j$. The Gaussian points and weights for the first two approximations are provided in Table 2.1.

Replacing the integral with a summation and omitting the emission term, the radiative transfer equation can be written as

$$\mu_i \frac{\mathrm{d}I(\tau, \mu_i)}{\mathrm{d}\tau} = I(\tau, \mu_i) - \frac{\varpi}{2} \sum_{j=-n}^{n} I(\tau, \mu_j) P(\mu_i, \mu_j) w_j - \frac{\varpi}{4\pi} F_\odot P(\mu_i, -\mu_0) \mathrm{e}^{-\tau/\mu_0}, \qquad i = -n, \ldots, n, \tag{2.25}$$

where the equation is discretized by replacing μ with μ_i $(-n, n)$, which represent the direction of the radiation streams.

The phase function may be numerically expended in Legendre polynomials with a finite number of terms N and can be expressed by

$$P(\mu_i, \mu_j) = \sum_{l=0}^{N} \varpi_l P_l(\mu_i) P_l(\mu_j), \qquad j = -n, \ldots, n. \tag{2.26}$$

Table 2.1 Gaussian points and weights.

n	2n	$\pm\mu_n$	w_n
1	2	$\mu_1 = 0.5773503$	$w_1 = 1$
2	4	$\mu_1 = 0.3399810$	$w_1 = 0.6521452$
		$\mu_2 = 0.8611363$	$w_2 = 0.3478548$

The discretized equation can then be rewritten as

$$\mu_i \frac{\mathrm{d}I(\tau, \mu_i)}{\mathrm{d}\tau} = I(\tau, \mu_i) - \frac{\varpi}{2} \sum_{l=0}^{N} \varpi_l P_l(\mu_i) \sum_{j=-n}^{n} I(\tau, \mu_j) P_l(\mu_j) w_j - \frac{\varpi}{4\pi} F_\odot \left[\sum_{l=0}^{N} (-1)^l \varpi_l P_l(\mu_i) P_l(\mu_0) \right] \mathrm{e}^{-\tau/\mu_0}. \tag{2.27}$$

In the discrete-ordinates method, analytical solutions for the diffuse intensity can be explicitly given for any optical depth. Moreover, useful approximations can be developed from this method for flux calculations. The two commonly used approximations of the discrete-ordinates method are the two-stream and four-stream approximations that are introduced in the following sections.

2.4.1. Two-Stream and Eddington's Approximation

Two-stream approximation for radiative transfer based on the discrete-ordinates method has been widely used in radiative flux calculations (Meador & Weaver, 1980) because analytic solutions for upward and downward fluxes can be derived and numerical computations for these fluxes can be efficiently performed.

In the two-stream approximation, two radiation streams, one upward and one downward, are selected, i.e., $N = 1$, and $j = -1$ and 1. A number of two-point quadrature methods have been developed for applications to two-stream radiative transfer (Meador & Weaver, 1980), including the delta-Eddington approximation (Joseph et al., 1976) and the Practical Improved Flux Method (PIFM; Zdunkowski et al., 1980), which used Gaussian quadratures with $\mu_1 = 0.5$ in the shortwave and $\mu_1 = 1/1.66$ in the longwave. Another commonly used Gaussian choice is shown in Table 2.1 (Liou, 1973, 1974) with $\mu_1 = 0.5773503$ and $w_1 = w_{-1} = 1$. Two equations can be obtained as follows after rearranging terms in equation (2.27) and denoting $I^\uparrow = I(\tau, \mu_1)$ and $I^\downarrow = I(\tau, -\mu_1)$

$$\mu_1 \frac{\mathrm{d}I^\uparrow}{\mathrm{d}\tau} = I^\uparrow - \varpi(1 - b)I^\uparrow - \varpi b I^\downarrow - S^- \mathrm{e}^{-\frac{\tau}{\mu_0}}, \tag{2.28}$$

$$\mu_1 \frac{\mathrm{d}I^\downarrow}{\mathrm{d}\tau} = I^\downarrow - \varpi(1 - b)I^\downarrow - \varpi b I^\uparrow - S^+ \mathrm{e}^{-\frac{\tau}{\mu_0}}. \tag{2.29}$$

where

$$g = \frac{\varpi_1}{3} = \frac{1}{2} \int_{-1}^{1} P(\cos\Theta) \cos\Theta \mathrm{d}\cos\Theta, \tag{2.30}$$

$$b = \frac{1 - g}{2} = \frac{1}{2} \int_{-1}^{1} P(\cos\Theta) \frac{1 - \cos\Theta}{2} \mathrm{d}\cos\Theta, \tag{2.31}$$

$$S^\pm = \frac{F_\odot \varpi}{4\pi}(1 \pm 3g\mu_1\mu_0), \tag{2.32}$$

where Θ is the scattering angle, $\cos\Theta = \mu\mu' + (1 - \mu^2)^{1/2} (1 - \mu'^2)^{1/2} \cos\phi$, and g is the asymmetry factor that is the first moment of the phase function. For isotropic scattering such as Rayleigh scattering, $g = 0$. The asymmetry factor increases as the diffraction peak of the phase function sharpens and more forward scattering occurs. The asymmetry factor may become negative if the phase function is peaked in backward direction (90°–180°). For Lorenz-Mie scattering where the phase function has a sharp peak at 0° scattering angle (forward direction), the asymmetry factor denotes the relative strength of forward scattering. The coefficients b and $1 - b$ represent the integrated fraction of back and forward scattered energy, respectively. Thus, the multiple scattering is represented in the two-stream approximation by the upward and downward intensities weighted by the appropriate fractions of the forward and backward phase functions.

Equations (2.28) and (2.29) are two first-order differential equations that can be solved analytically and the details can be found in Liou (2002). The solutions are given as

$$I^{\uparrow} = I(\tau, \mu_1) = Kv e^{k\tau} + Hu e^{-k\tau} + \varepsilon e^{-\tau/\mu_0}, \tag{2.33}$$

$$I^{\downarrow} = I(\tau, -\mu_1) = Ku e^{k\tau} + Hv e^{-k\tau} + \gamma e^{-\tau/\mu_0}, \tag{2.34}$$

where

$$v = (1 + a)/2, \quad u = (1 - a)/2$$

$$a^2 = (1 - \varpi)/(1 + \varpi g),$$

$$\varepsilon = (\alpha + \beta)/2, \quad \gamma = (\alpha - \beta)/2$$

$$\alpha = Z_1 \mu_0^2 / \left(1 - \mu_0^2 k^2\right) \quad \beta = Z_2 \mu_0^2 / \left(1 - \mu_0^2 k^2\right), \tag{2.35}$$

$$Z_1 = \frac{(1 - \varpi g)(S^- + S^+)}{\mu_1^2} + \frac{S^- - S^+}{\mu_1 \mu_0},$$

$$Z_2 = \frac{(1 - \varpi)(S^- - S^+)}{\mu_1^2} + \frac{S^- + S^+}{\mu_1 \mu_0},$$

$$k^2 = (1 - \varpi)(1 - \varpi g)/\mu_1^2,$$

where $\pm k$ are the eigenvalues for the solution of the differential equations, u and v represent the eigenfunctions defined by the similarity parameter a. The constants K and H are to be determined from the diffuse radiation boundary conditions at the top and the bottom of the scattering layer. Assuming no diffuse radiation from the top and the bottom, we have

$$K = -\left(\varepsilon v e^{-\tau/\mu_0} - \gamma u e^{-\tau/\mu_0}\right) / \left(v^2 e^{k\tau_1} - u^2 e^{-k\tau_2}\right), \tag{2.36}$$

$$H = -\left(\varepsilon u e^{-\tau/\mu_0} - \gamma v e^{-\tau/\mu_0}\right) / \left(v^2 e^{k\tau_1} - u^2 e^{-k\tau_2}\right). \tag{2.37}$$

Once the upward and downward intensities have been evaluated, the upward and downward fluxes can be computed as

$$F^{\uparrow}(\tau) = 2\pi \mu_1 I^{\uparrow}, \tag{2.38}$$

$$F^{\downarrow}(\tau) = 2\pi \mu_1 I^{\downarrow}. \tag{2.39}$$

The Eddington's approximation uses an approach similar to that of the two-stream approximation and was originally used for studies of radiative equilibrium in stellar atmosphere (Eddington, 1916). In this approximation, the radiative transfer equation is decomposed using the property of Legendre polynomials. In line with the Legendre polynomial expansion for the phase function denoted in equation (2.26), the diffuse radiative intensity may be expanded in terms of Legendre polynomials such that

$$I(\tau, \mu) = \sum_{l=0}^{N} I_l(\tau) P_l(\mu). \tag{2.40}$$

Letting $N = 1$, the basic radiative transfer equation (2.16) can be reduced to a set of two simultaneous equations similar to equations (2.29) and (2.30), which can be analytically solved and the solutions are similar to those of the two-stream approximation.

Combining two-stream approximation for discrete-ordinates method and the Eddington's approximation, a generalized two-stream approximation may be expressed by

$$\frac{dF^{\uparrow}(\tau)}{d\tau} = \gamma_1 F^{\uparrow}(\tau) - \gamma_2 F^{\downarrow}(\tau) - \gamma_3 \varpi F_{\odot} e^{-\tau/\mu_0}, \tag{2.41}$$

$$\frac{dF^{\downarrow}(\tau)}{d\tau} = \gamma_2 F^{\uparrow}(\tau) - \gamma_1 F^{\downarrow}(\tau) + (1 - \gamma_3) \varpi F_{\odot} e^{-\tau/\mu_0}. \tag{2.42}$$

The coefficients γ_i are provided in Table 2.2. In the two-stream approximation, there are only upward and downward intensities in the directions μ_1 and $-\mu_1$, while the phase function is expanded in two terms in Legendre polynomials. In Eddington's approximation, both the intensity and phase functions are expanded in two polynomials terms.

The solutions for the equations of the generalized two-stream approximation are as follows:

$$F^{\uparrow} = vK e^{k\tau} + uH e^{-k\tau} + \varepsilon e^{-\tau/\mu_0}, \tag{2.43}$$

$$F^{\downarrow} = uK e^{k\tau} + vH e^{-k\tau} + \gamma e^{-\tau/\mu_0}, \tag{2.44}$$

Table 2.2 Coefficients in two-stream approximations.

Method	γ_1	γ_2	γ_3
Two-Stream	$[1 - \varpi(1 + g)/2]/\mu_1$	$\varpi(1 - g)/2\mu_1$	$(1 - 3g\ \mu_1\mu_0)/2$
Eddington's	$[7 - (4 + 3g)\varpi]/4$	$-[1 - (4 - 3g)\varpi]/4$	$(2 - 3g\ g\mu_0)/4$

where coefficients K and H can be determined from boundary conditions, and

$$k^2 = \gamma_1^2 - \gamma_2^2,$$

$$\upsilon = \frac{1}{2}\left[1 + \frac{\gamma_1 - \gamma_2}{k}\right], \qquad u = \frac{1}{2}\left[1 - \frac{\gamma_1 - \gamma_2}{k}\right], \tag{2.45}$$

$$\varepsilon = [\gamma_3(1/\mu_0 - \gamma_1) - \gamma_2(1-\gamma_3)]\mu_0^2 \varpi F_\odot,$$

$$\gamma = -[(1-\gamma_3)(1/\mu_0 + \gamma_1) - \gamma_2\gamma_3]\mu_0^2 \varpi F_\odot.$$

2.4.2. Four-Stream Approximation

The four-stream approximation, which is first derived by Liou (1974), is also based on the discrete-ordinates method for radiative transfer. A systematic solution for this approximation has been presented by Liou et al. (1988).

If we consider four radiative streams, with two streams in the upward and downward directions, respectively, i.e., $n=2$, and expand the phase function in four terms, i.e., $N=3$, then we can obtain four first-order differential equations:

$$\frac{d}{d\tau}\begin{bmatrix} I_2 \\ I_1 \\ I_{-1} \\ I_{-2} \end{bmatrix} = \begin{bmatrix} b_{2,-2} & b_{2,-1} & b_{2,1} & b_{2,2} \\ b_{1,-2} & b_{1,-1} & b_{1,1} & b_{1,2} \\ -b_{1,2} & -b_{1,1} & -b_{1,-1} & -b_{1,-2} \\ -b_{2,2} & -b_{2,1} & -b_{2,-1} & -b_{2,-2} \end{bmatrix} \times \begin{bmatrix} I_2 \\ I_1 \\ I_{-1} \\ I_{-2} \end{bmatrix} - \begin{bmatrix} b_{2,-0} \\ b_{1,-0} \\ b_{-1,-0} \\ b_{-2,-0} \end{bmatrix}, \tag{2.46}$$

where the terms $b_{i,j}$ ($i=\pm1, 2; j=-0, \pm1, 2$) are defined as follows:

$$b_{i,j} = \begin{cases} c_{i,j/\mu_i} \\ (c_{i,j} - 1)/\mu_i \end{cases}$$

$$c_{i,j} = \frac{\varpi}{2} w_j P(\mu_i, \mu_j) = \frac{\varpi}{2} w_j \sum_{l=0}^{N} \varpi_l P_l(\mu_i) P_l(\mu_j),$$

$$j = -n, \ldots, -0, \ldots n, \tag{2.47}$$

$$c_{i,-j} = c_{-i,j}, \qquad c_{-i,-j} = c_{i,j}, \qquad i \neq -0.$$

The Gauss quadrature and weights in the four-stream approximation are $\mu_1 = 0.3399810$, $\mu_2 = 0.8611363$, and $w_1 = 0.6521452$, $w_2 = 0.3478548$, as listed in Table 2.1. The four-by-four matrix represents the contribution of multiple scattering. Thus, the derivative of the diffuse intensity at a specific quadrature angle is the weighted sum of the multiple-scattered intensity from all four quadrature angles. The last term represents the contribution of the unscattered component of the direct flux.

The four equations can be analytically solved with solutions to be

$$\begin{bmatrix} I_1 \\ I_{-1} \\ I_2 \\ I_{-2} \end{bmatrix} = \begin{bmatrix} \Phi_1^+ e_1^- & \Phi_1^- e_1^+ & \Phi_2^+ e_2^- & \Phi_2^- e_2^+ \\ \Phi_1^- e_1^- & \Phi_1^+ e_1^+ & \Phi_2^- e_2^- & \Phi_2^+ e_2^+ \\ \phi_1^+ e_1^- & \phi_1^- e_1^+ & \phi_2^+ e_2^- & \phi_2^- e_2^+ \\ \phi_1^- e_1^- & \phi_1^+ e_1^+ & \phi_2^- e_2^- & \phi_2^+ e_2^+ \end{bmatrix} \begin{bmatrix} G_1 \\ G_{-1} \\ G_2 \\ G_{-2} \end{bmatrix} + \begin{bmatrix} Z_1^+ \\ Z_1^- \\ Z_2^+ \\ Z_1^- \end{bmatrix} e^{-\tau/\mu_0}, \tag{2.48}$$

where the elements $e_1^- = e^{-k_1\tau}, e_1^+ = e^{k_1\tau}, e_2^- = e^{-k_2\tau}$, and $e_2^+ = e^{k_2\tau}$. The eigenvectors are

$$\phi_{1,2}^{\pm} = \frac{1}{2}\left(1 \pm \frac{b_{11}^- - A_{1,2}b_{21}^-}{a^-} k_{1,2}\right), \tag{2.49a}$$

$$\Phi_{1,2}^{\pm} = \frac{1}{2}\left(A_{1,2} \pm \frac{A_{1,2}b_{22}^- - b_{12}^-}{a^-} k_{1,2}\right). \tag{2.49b}$$

where $b_{ij}^{\pm}$ is defined by

$$b_{22}^{\pm} = b_{2,2} \pm b_{2,-2}, \qquad b_{21}^{\pm} = b_{2,1} \pm b_{2,-1}, \tag{2.50a}$$

$$b_{12}^{\pm} = b_{1,2} \pm b_{1,-2}, \qquad b_{11}^{\pm} = b_{1,1} \pm b_{1,-1}, \tag{2.50b}$$

$k_{1,2}$ are eigenvalues determined by

$$k^2 = [b \pm (b^2 + 4c)^{1/2}]/2, \tag{2.51}$$

where $b = a_{22} + a_{11}, c = a_{21}a_{12} - a_{11}a_{22}, A_{1,2} = (k_{1,2}^2 - a_{22})/a_{21}$, a_{ij} are defined by

$$a_{22} = b_{22}^+ b_{22}^- + b_{12}^+ b_{21}^-, \qquad a_{21} = b_{21}^+ b_{22}^- + b_{11}^+ b_{21}^-, \tag{2.52a}$$

$$a_{12} = b_{22}^+ b_{12}^- + b_{12}^+ b_{11}^-, \qquad a_{11} = b_{21}^+ b_{12}^- + b_{11}^+ b_{11}^-, \tag{2.52b}$$

and $a^- = b_{22}^- b_{11}^- - b_{12}^- b_{21}^-$. The Z functions are defined by

$$Z_{1,2}^{\pm} = \frac{1}{2}\left(\eta_{1,2} + \eta'_{1,2}\right), \tag{2.53}$$

where $\eta_{1,2}$ and $\eta'_{1,2}$ are defined by

$$\begin{aligned} \eta_1 &= \frac{d_1/\mu_0^2 + a_{12}d_2 - a_{22}d_1}{f(1/\mu_0)} \frac{F_\odot}{2\pi}, \\ \eta_2 &= \frac{d_2/\mu_0^2 + a_{21}d_1 - a_{11}d_2}{f(1/\mu_0)} \frac{F_\odot}{2\pi}, \\ \eta'_1 &= \frac{d'_1/\mu_0^2 + a'_{12}d'_2 - a'_{22}d'_1}{f(1/\mu_0)} \frac{F_\odot}{2\pi}, \\ \eta'_2 &= \frac{d'_2/\mu_0^2 + a'_{21}d'_1 - a'_{11}d'_2}{f(1/\mu_0)} \frac{F_\odot}{2\pi}. \end{aligned} \tag{2.54}$$

The function f is defined as

$$f(k) = k^4 - bk^2 - c, \tag{2.55}$$

where k is replaced by $1/\mu_0$. d_i are defined by

$$d_1 = b_{12}^- b_2^- + b_{11}^- b_1^- + b_1^+/\mu_0, \tag{2.56a}$$

$$d_2 = b_{22}^- b_2^- + b_{21}^- b_1^- + b_2^+/\mu_0. \tag{2.56b}$$

d_i' and a_{ij}' have the same expressions as those for d_i and a_{ij} except that the superscripts + and – are replaced by – and +, respectively. The coefficients G_j ($j = 1, 2, -1, -2$) can be determined from boundary conditions. Once the intensities for the four streams have been obtained, the upward and downward fluxes at a given τ are given by

$$F^{\uparrow}(\tau) = 2\pi(w_1\mu_1 I_1 + w_2\mu_2), \tag{2.57}$$

$$F^{\downarrow}(\tau) = 2\pi(w_1\mu_1 I_{-1} + w_2\mu_2 I_{-2}) + \mu_0 F_{\odot} e^{-\tau/\mu_0}. \tag{2.58}$$

2.4.3. Delta-Function Adjustment

When calculating the radiative transfer in the atmosphere, the effects of scattering and absorption by clouds and various aerosols must be included. These particles usually have size larger than the incident solar radiation, and in many cases a sharp diffraction occurs near 0° scattering angle. To incorporate the forward peak contribution in multiple scattering, we may consider an adjusted absorption and scattering atmosphere such that the fraction (f) of scattered energy in the forward peak is accounting for. Using delta-Eddington scaling, $f = g^2$ (Joseph et al., 1976). The forward peak can be expressed as $f = \varpi_2/5$ ($l = 1$) for two-stream approximation and $f = \varpi_4/9$ ($l = 4$) for four-stream approximation, to account for strong forward scattering by cloud and aerosol particles. For M-stream, the delta-M method, which is a natural extension of the delta-Eddington approximation developed by Wiscombe (1977), can be applied to all orders M of angular approximation. The delta-M method relies on matching the first $2M$ phase moments and using a Dirac delta-function representation of forward scattering.

We use primes to represent the adjusted single-scattering properties, optical depth τ, single-scattering albedo ϖ, and phase function P or asymmetry factor g. The optical depth is the sum of the scattering (τ_s) and absorption (τ_a) optical depth. Since the forward peak is only associated with scattering without the contribution of absorption, the adjusted scattering and absorption optical depth must be

$$\tau_s' = (1 - f)\tau_s, \tag{2.59}$$

$$\tau_a' = \tau_a. \tag{2.60}$$

The total adjusted optical depth is then

$$\tau' = \tau_s' + \tau_s' = (1 - f)\tau_s + \tau_a = \tau(1 - f\varpi), \tag{2.61}$$

where the single-scattering albedo by definition can be expressed by $\varpi = \tau_s/\tau$. The adjusted single-scattering albedo is defined by

$$\varpi' = \frac{\tau_s'}{\tau'} = \frac{(1 - f)\tau_s}{(1 - f\varpi)\tau} = \frac{(1 - f)\varpi}{1 - f\varpi}. \tag{2.62}$$

Moreover, we may express the normalized phase function expansion by incorporating the δ-forward adjustment in the form

$$P_l(\cos\Theta) = 2f\delta(\cos\Theta - 1) + (1 - f)\sum_{l=0}^{N}\varpi_l' P_l(\cos\Theta), \tag{2.63}$$

where δ denotes the delta-function, and ϖ_l' is the adjusted coefficients in the phase function expansion. The adjusted phase function is then given by

$$P'(\cos\Theta) = \sum_{l=0}^{N}\varpi_l' P_l(\cos\Theta). \tag{2.64}$$

Equations (2.61), (2.62), and (2.64) constitute the generalized similarity principle for radiative transfer. That is, the removal of the forward diffraction peak in scattering processes using adjusted single-scattering parameters is "equivalent" to actual scattering processes.

The similarity principle was first introduced by Sobolev (1975) for isotropic scattering. The inclusion of the asymmetry factor was discussed by van de Hulst (1980). The principle of employing a Dirac delta-function to approximate highly forward peaked scattering in radiative transfer has been presented by Hansen (1969), Potter (1970), and Wiscombe (1977).

2.4.4. Application to Plane-Parallel Atmosphere

The accuracy of the radiative transfer approximations described in the previous sections has been examined by comparing the approximate results with the values computed from the "exact" method, such as the adding method. Figure 2.6 shows the relative accuracy of the delta-two-stream (upper panel) and delta-four-stream (lower panel) approximations with respect to the results derived from the adding method displayed in intervals of 0%, 1%, 2%, 5%, 10%, etc. Here, the relative accuracy is defined by $(\Delta r/r)100\% = [(\hat{r} - r)r]100\%$, where $\hat{r}$ and r represent the reflectance computed from the approximation and the "exact" method, respectively. Likewise, the relative accuracy of the total transmittance is denoted by $(\Delta t/t)100\%$. In general, reflectance and total transmittance values computed from the delta-four-stream approximation are accurate within about 5%, while the delta-two-stream approximation produces errors greater than 5%–10%. In particular, errors of more than 50%

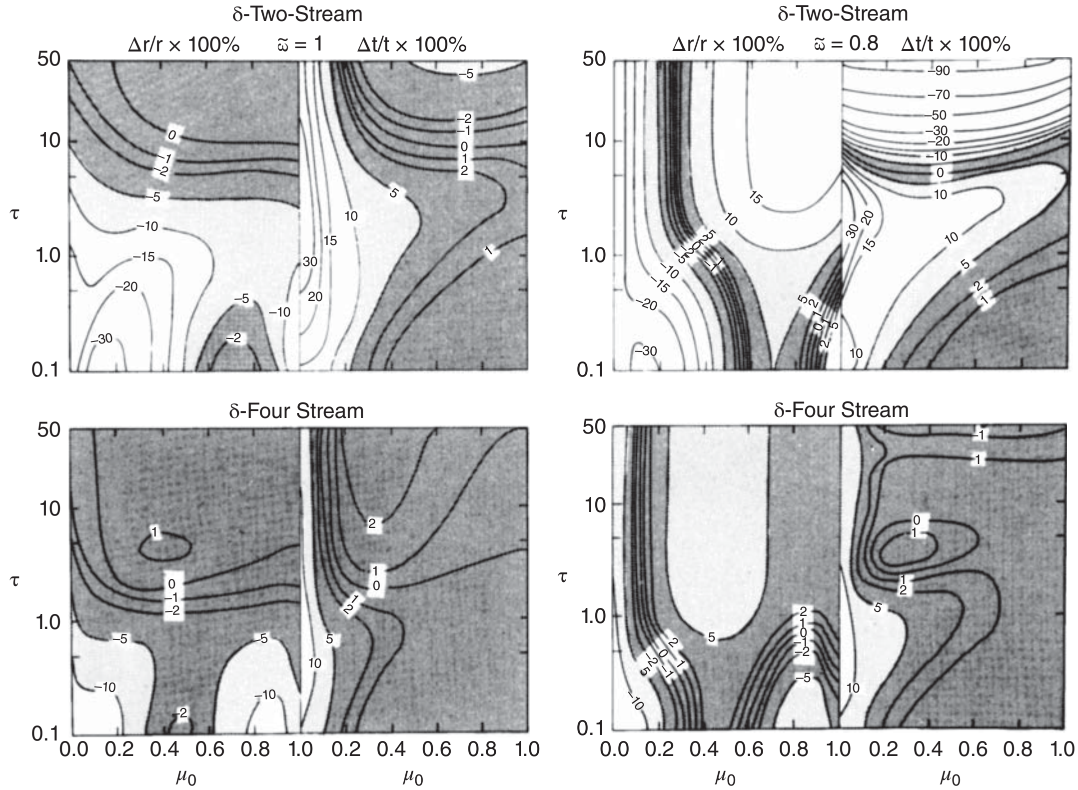

Figure 2.6 Relative accuracy of the reflectance and transmittance computed from the delta-two-stream (upper panel) and delta-four-stream (lower panel) approximations with respect to the results derived from the adding method, for $\varpi = 1$ (conservative scattering, left panel) and $\varpi = 0.8$ (right panel), respectively. The results are shown in the domain of τ (ranging from 0.1 to 50) and μ_0 (0.0–1.0), and expressed in terms of percentage. The heavy and light shadings denote errors with 5% and 5%–10%, respectively, while the white area represent errors larger than 10%. Source: Liou et al. (1988)/American Meteorological Society.

may occur in the case of large optical depth for the delta-two-stream when $\varpi = 0.8$. The accuracy of the delta-two-stream approximation shown in Figure 2.6 is comparable to that of the delta-Eddington approximation reported by King and Harshvardhan (1986).

For application to the solar absorption bands, in which gaseous absorption in scattering atmospheres must be accounted for, the accuracy of the delta-two-stream and delta-four-stream approximations has also been examined using single-scattering albedo of 0.5 and 0.3. For cases involving large absorption, the reflectance values are generally very small. Thus, we investigate the relative accuracy for the absorptance, defined as $(\Delta A/A)100\%$, where $A = 1 - r - t$. Figure 2.7 shows that the delta-four-stream approximation produces better accuracy than the delta-two-stream approximation, with errors for acceptance generally less than 2%. The accuracy increases as ϖ decreases because the effect of multiple scattering on the flux calculations becomes less important. For total transmittance, errors from the delta-four-stream approximation are again within 5%. Large relative errors can be produced by the delta-two-stream approximation when the transmittance values are small.

Stephens et al. (2001) assessed a select number of two-stream models in representing solar and infrared radiative transfer problems. They reported that the delta-Eddington model and the constant-hemispheric two-stream models are shown to be superior to other two-stream methods of solution and also superior to four-stream solutions for the many classes of problems relevant to modeling the global atmosphere. Räisänen (2002) tested four two-stream approximations, including the delta-Eddington approximation (Joseph et al., 1976), the PIFM (Zdunkowski et al., 1980), and two recent modifications of delta-Eddington by Li (1999) and Qiu (1999), with the general circulation model (GCM) data set. It is found that two-stream approximations generally performed fairly well with a negative bias in atmospheric absorption and a positive bias in surface net shortwave flux of about 1 W M^{-2} in the global mean. Furthermore, the absorption errors depended substantially on solar elevation. The tests with GCM data also confirmed

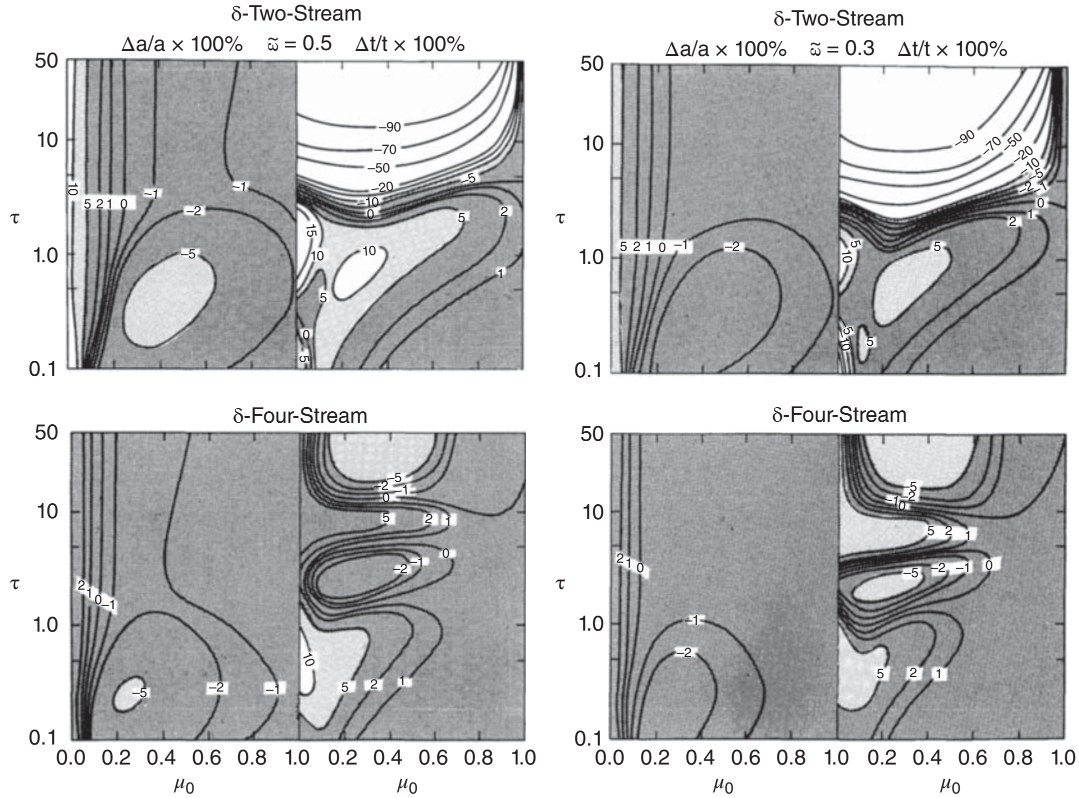

Figure 2.7 Same as Figure 2.6, except for absorptance. The left and right panels are for $\varpi = 0.5$ and $\varpi = 0.3$, respectively. Source: Liou et al. (1988)/American Meteorological Society.

that the four-stream method is considerably more accurate than the two-stream approximations, especially for atmospheric absorption.

While all approximations for radiative transfer calculations have advantages and shortcomings in terms of the computational accuracy, the delta-four-stream approximation can achieve relative accuracy with 5% for all reasonable ranges of single-scattering parameters at a given wavelength. For computations of solar fluxes covering the entire solar spectrum, the averaged accuracy should also be within 5%. The delta-four-stream approximation has all the radiative characteristics inherent in the delta-two-stream approximation, and the solution is also in analytic form so that the computer time involved is reasonable. For radiative transfer parameterizations in numerical models, the delta-four-stream approximation would be an excellent method. Two-stream approximations are currently employed for multiple-scattering calculations in most solar radiation schemes used in climate models. Fu et al. (1997) demonstrated that the delta-two-stream method is the most computationally efficient but produces significant errors in fluxes and heating rates under cloudy conditions. High accuracy can be obtained by using the delta-four-stream method, but substantial computer time is required for the calculation of thermal infrared radiative transfer. The delta-two/four-stream combination method is sufficiently economical for thermal IR calculations; it is 4 times faster than the delta-four-stream method but only 50% slower than the two-stream method and at the same time produces acceptable accuracy under most atmospheric conditions.

2.5. RADIATION-CLOUD INTERACTIONS IN LARGE-SCALE ATMOSPHERIC MODELS

Clouds absorb, reflect, and transmit solar radiation, and the amount is a function of the optical depth, the geometry governing the Sun, and the direction of detection. Clouds can also reflect and transmit the thermal infrared radiation emitted from the surface and the atmosphere and, meanwhile, emit thermal IR radiation according to the temperature structure within the clouds. While considerable advances in the understanding of atmospheric processes and feedbacks in the climate system have led to a better representation of these mechanisms in general circulation models, the greatest uncertainty in predictability of future climate arises from clouds and their interactions with radiation.

Theoretical, observational, and modeling studies have demonstrated the important role of cloud-radiation interactions in climate variability. Role of clouds in climate has twofold: first clouds are generated by large-scale dynamic forcing, radiative cooling in the atmosphere, and turbulent transfer at the surface. On the other hand, clouds provide one of the most important mechanisms for the vertical redistribution of momentum, moisture, and sensible and latent heat. Clouds also influence the coupling between the atmosphere and the surface, as well as the radiative and dynamical and hydrological balance. The atmospheric general circulation model (AGCM) studies of Ramanathan et al. (1983), Slingo and Slingo (1988, 1991), and Randall et al. (1989) have shown that radiation, latent heat release, and small-scale transport are of equal importance in the cloud-climate problem and that many features of the simulated climate are sensitive to the treatment of clouds and radiation in the model. The cloud-radiation interaction and feedback problem have been identified as the highest priority item in climate research nationally and internationally, as illustrated by a number of composite field and satellite observations, including the International Satellite Cloud Climatology Project (ISCCP), the First ISCCP Regional Experiment (FIRE), the Atmospheric Radiation Measurement (ARM) Program, and the Earth Radiation Budget Experiment (ERBE). Therefore, numerical models used for climate studies are required to provide the cloud and radiation fields as accurate as possible. Recent comparisons of feedbacks produced by climate models under climate change show that the current generation of models still exhibits a large spread in cloud feedbacks, which is larger than for other feedbacks (Bony et al., 2006). Webb et al. (2013) diagnosed climate feedback parameters including rapid adjustment in 12 atmosphere/mixed-layer-ocean climate models and found that cloud effects can explain the full range of climate sensitivities, and cloud feedback components contribute 4 times as much as cloud components of CO_2 forcing to the range.

The parameterization of cloud-radiation processes in climate models is a complex task. Radiative transfer in the atmosphere is determined by spectrally dependent optical properties. Calculation of the radiative heating/cooling in clouds is complicated due to difficulties in parameterizing their single-scattering properties, especially those of ice clouds due to complexities in the ice crystal size, shape, and orientation, which cannot be determined from the models (Liou, 1986). Furthermore, clouds have a typical length scale of perhaps several hundred meters and display substantial horizontal variability on scales that are generally smaller than the usual AGCM grid box. A specific challenge in studying the cloud-radiation feedback on climate is to estimate the uncertainty in the vertical profile of cloud cover, the information of which is limited in present satellite and surface observations. In recent years, some models have improved representation of subgrid scale cloud variability, which has important effects on grid-mean radiative fluxes, for example, based on the use of probability density functions of thermodynamic variables (e.g., Watanabe et al., 2009). Stochastic approaches have also been used to efficiently account for this variability (Barker et al., 2008). Improved treatments of overlap have been developed in some models based on new observations that show cloud layers at different levels overlap less often than typically assumed in GCMs (Pincus et al., 2006; Shonk et al., 2012).

2.5.1. Parameterization of Cloud Radiative Properties

Clouds are conventionally classified in terms of their position and appearance in the atmosphere. For radiative transfer calculations, we normally classify clouds as water cloud at temperature above 0 °C, ice below about −38 °C (e.g., Koop et al., 2000), and either or both phases at intermediate temperatures. Low clouds with height <2 km are normally water clouds. High clouds present at height >6 km are normally ice clouds. In between are the middle clouds that could consist of both water and ice clouds. Under the plane-parallel assumption, the radiative transfer methods introduced in section 2.4 can be applied to clouds. We have learned from section 2.2 that the fundamental parameters in radiative transfer are the single-scattering properties, including extinction coefficient, single-scattering albedo, and phase function or asymmetry factor. In the case of clouds, the basic extinction properties are determined by particle size distribution.

The calculations of the single-scattering properties require a detailed light scattering program and particle size distribution and are usually time consuming. If radiation calculations are for an evolving cloud where particle size distribution varies as a function of time and/or space, the computer time needed just for determining the single-scattering properties would be formidable even with a supercomputer. Thus, it is practically required to simplify the computational procedure for the calculations of the single-scattering properties of cloud particles.

Water Clouds

The characteristics of scattered light from clouds depend on the droplet size distribution, $n(r)$. Therefore, the first parameter describing droplet size distribution should be some measure of the mean size. For water clouds, since the spherical droplets scatter an amount of light in proportion to their cross-sectional area, we may define a mean effective radius r_e, which differs from simple mean radius by using droplet cross section as a weight factor:

$$r_e = \frac{\int r \cdot \pi r^2 n(r)\mathrm{d}r}{\int \pi r^2 n(r)\mathrm{d}r}. \tag{2.65}$$

From the definition of liquid water content (LWC), the liquid water path (LWP), which is the vertically integrated LWC over a cloud thickness of Δz, can be expressed in terms of droplet radius as

$$\mathrm{LWP} = \Delta z \cdot \mathrm{LWC} = \Delta z \cdot \rho_l V = \Delta z \cdot \rho_l \cdot \frac{4\pi}{3} \int r^3 n(r)\mathrm{d}r, \tag{2.66}$$

where ρ_l is the density of liquid water and V is the volume of cloud droplets divided by the volume of air. The cloud optical depth for a given droplet size distribution can also be expressed as a function of droplet radius by

$$\tau = \Delta z \int \sigma_e n(r)\mathrm{d}r = \Delta z \int Q_e \pi r^2 n(r)\mathrm{d}r, \tag{2.67}$$

where the extinction cross section $\sigma_e = Q_e \pi r^2$, and Q_e is the efficiency factor that is a function of the droplet radius, wavelength, and refractive index. For visible wavelength, $Q_e \cong 2$ for cloud droplets. Therefore, the mean effective radius r_e (μm) can be related to LWP (g cm^{-2}) and τ in the form

$$r_e \cong \frac{3}{2}\mathrm{LWP}/\tau, \quad \text{or} \quad \tau = \frac{3}{2}\mathrm{LWP}/r_e. \tag{2.68}$$

That is, the cloud optical depth can be obtained once the cloud effective radius is known.

The single-scattering albedo is defined by

$$1 - \varpi = \sigma_a/\sigma_e, \tag{2.69}$$

where σ_a denotes the absorption cross section, which is proportional to the product of the absorption coefficient k and the volume, and it follows that $\sigma_a = k \cdot \frac{4}{3} r_e \int \pi r^2 n(r)\mathrm{d}r$. If an efficiency factor of 2 is used for extinction, then $\sigma_e = 2 \int \pi r^2 n(r)\mathrm{d}r$. The other important factor is asymmetry factor. Based on Mie scattering calculations, the asymmetry factor shows relatively little variation in the solar wavelength.

Parameterization of the solar radiative properties for water clouds has been carried out by Stephens (1978), Liou and Wittman (1979), and Slingo (1989). Based on a number of droplet size distributions, the optical depth, single-scattering albedo, and asymmetry factor, which are all functions of wavelength and position, can be expressed in terms of r_e. Slingo (1989) has developed a solar radiative transfer parameterization scheme based on the two-stream approximation, in which both LWP and r_e are used as the basic parameters for the computation of the spectral solar radiative properties of water clouds. However, this parameterization was designed for a limited cloud droplet size range of 4.2–16.6 μm. Dobbie et al. (1999) have shown that the Slingo (1989) parameterization does not agree with calculations based on Mie theory for large cloud droplets. Nielsen et al. (2014) proposed a new cloud liquid optical property scheme based on the Mie solution to Maxwell's equations (Wiscombe, 1980) in the form

$$\beta(\lambda, x, y, z) = a(\lambda) r_e(x, y, z)^{-b(\lambda)}, \tag{2.70}$$

$$\varpi(\lambda, x, y, z) = c(\lambda) - d(\lambda) r_e(x, y, z), \tag{2.71}$$

$$\mathrm{g}(\lambda, x, y, z) = e(\lambda) + f(\lambda) r_e(x, y, z) - h(\lambda)\exp[-j(\lambda) r_e], \tag{2.72}$$

where a–f, h, and j are coefficients that can be determined from numerical fittings based on detailed light scattering and absorption calculations for a range of ice crystal size distributions and shapes.

Ice Clouds

Parameterization for ice clouds can be obtained following the similar procedure. Ice crystals are nonspherical, and ice crystal size distributions are usually expressed in terms of the maximum dimension (or length) L. Representation of the size distribution for ice crystals is much more involved than that for water droplets. To the extent that scattering of light is proportional to the cross-section area of nonspherical particles, we may define a mean effective size D_e, analogous to the mean effective radius r_e, to represent ice crystal size distributions in the form

$$D_e = \frac{\int D \cdot DLn(L)\mathrm{d}l}{\int DLn(L)\mathrm{d}l}, \tag{2.73}$$

where D is the width of the particle, $n(L)$ denotes the ice crystal size distribution, and the numerator and denominator represent the volume-weighted and area-weighted ice crystal size distributions, respectively.

The ice water content (IWC) for a given ice crystal size distribution $n(L)$ is defined by

$$\mathrm{IWC} = \int V_i \rho_i n(L)\mathrm{d}L, \tag{2.74}$$

where ρ_i is the density of ice, and V_i is the volume of an individual ice crystal. Considering a hexagonal ice crystal, the volume is given by

$$V_i = \frac{3\sqrt{3}}{8} LD^2. \tag{2.75}$$

The ice water path (IWP) for a cloud with thickness Δz is then IWP = $\Delta z \cdot$IWC.

The optical depth for ice clouds is defined by

$$\tau = \Delta z \int \sigma_e n(L)\mathrm{d}L. \tag{2.76}$$

For randomly oriented hexagonal ice crystals in the limits of geometric optics, the extinction cross section may be expressed by (Takano & Liou, 1989)

$$\sigma_{\mathrm{e}} = \frac{3}{2}D\left(\frac{\sqrt{3}}{4}D + L\right). \tag{2.77}$$

Using all the preceding equations, the optical depth can be determined by two independent cloud physics variables, IWP and D_{e}, as

$$\tau \simeq \mathrm{IWP}\left(a + \frac{b}{D_{\mathrm{e}}}\right), \tag{2.78}$$

where a and b are certain coefficients.

The absorption cross section is approximately proportional to the product of the absorption coefficient k and the volume for weak absorption. Thus, the single-scattering albedo for randomly oriented hexagonal ice crystals may be parameterized in the form

$$1 - \varpi = \frac{\sigma_{\mathrm{a}}}{\sigma_{\mathrm{e}}} \sim \frac{k\sqrt{3}LD^2}{D\left(\sqrt{3}D + 4L\right)}. \tag{2.79}$$

Based on aircraft observations by Ono (1969) and Auer and Veal (1970), the width D may be related to the length L. Thus, $1 - \varpi$ must be proportional to the mean effective size as

$$1 - \varpi \simeq c + dD_{\mathrm{e}}, \tag{2.80}$$

where c and d are certain coefficients.

In the preceding discussion, the linear relationship derived are based on the geometric optics limit and the assumptions that the ice crystals are randomly oriented in space and their absorption is weak. For general cases, we would expect that higher-order expansion may be needed to define more precisely the single-scattering properties of ice crystals in terms of D_{e}. Thus, general parameterizations of single-scattering properties involving ice clouds may be written in the forms

$$\tau_i = \left(\sum_{n=0}^{N}\frac{a_{n,i}}{D_{\mathrm{e}}^n}\right)\mathrm{IWP}, \tag{2.81}$$

$$1 - \varpi_i = \sum_{n=0}^{N} b_{n,i}D_{\mathrm{e}}^n, \tag{2.82}$$

where the subscript i denotes the index for the spectral band, a_n and b_n are empirical coefficients that must be determined from numerical fittings with detailed light scattering calculations, and N is the total number of expansion terms to achieve a certain accuracy. The asymmetry factor may also be expressed in a likely expansion as

$$\mathrm{g}_i = \sum_{n=0}^{N} c_{n,i}D_e^n, \tag{2.83}$$

where c_n are again empirical coefficients. Based on numerical experiments, it is found that for solar bands the first-order polynomial expansion ($N = 1$) is sufficient to achieve 0.1% accuracy. However, for thermal infrared bands, the second-order polynomial fitting ($N = 2$) is required to achieve this level of accuracy (Fu & Liou, 1993).

Ice clouds consist of ice crystals with complex shapes and sizes. Figure 2.8 shows the observed ice crystal size

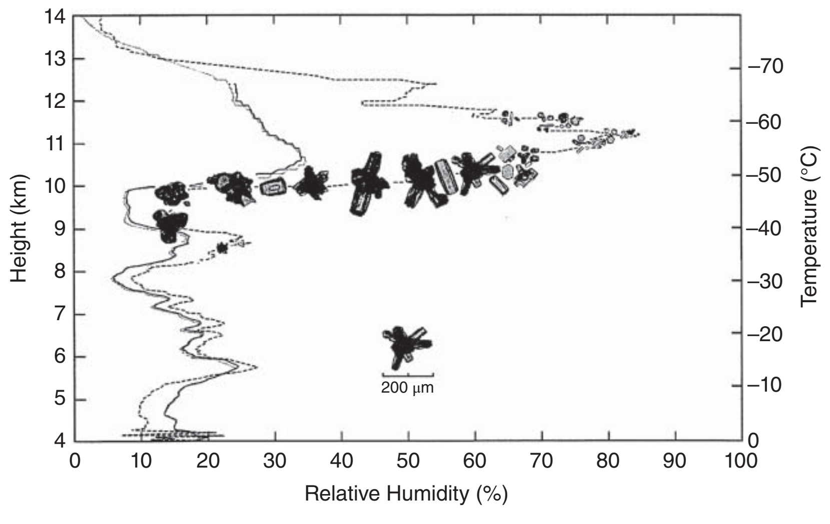

Figure 2.8 Ice crystal size and shape as a function of height and relative humidity captured by a replicator balloon sounding system in Marshall, Colorado on 10 November 1994. The relative humidity was measured by cryogenic hygrometer (dashed line) and Vaisala RS80 instruments (solid line and dots). Also shown is temperature as a function of height. Source: Courtesy of Andrew Heymsfield.

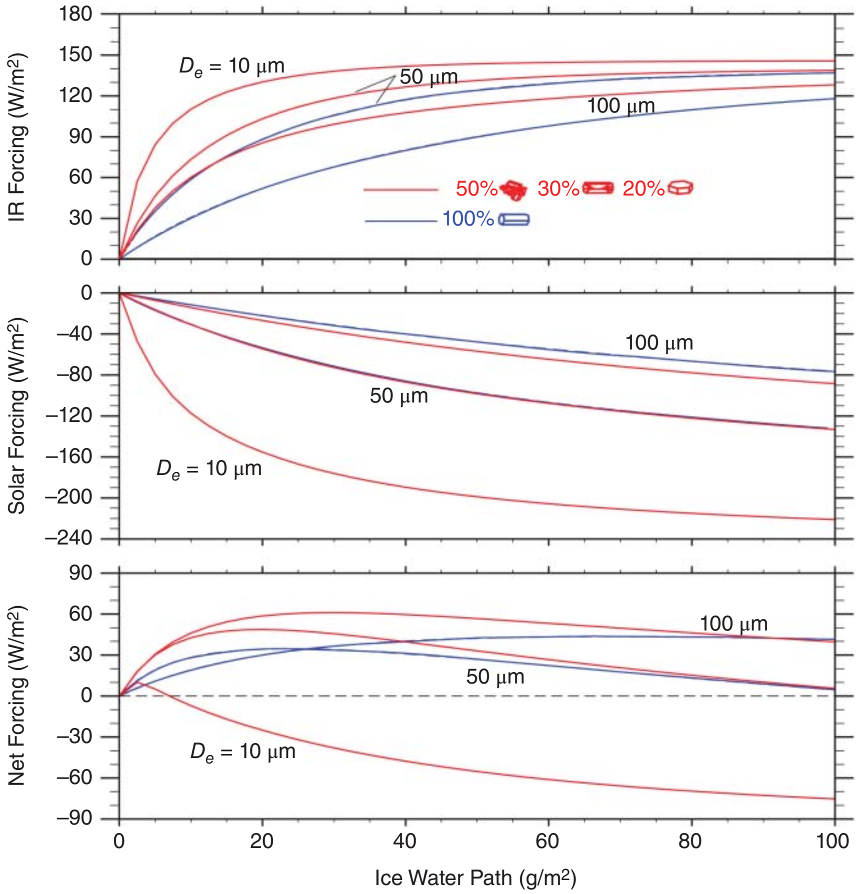

Figure 2.9 Solar, thermal IR, and net radiative forcings for cirrus clouds as functions of mean effective size D_e and ice water path for two ice crystal shape distributions in the standard atmospheric condition. The solar constant, solar zenith angle, surface albedo, cloud base height, and cloud thickness used in the calculations are 1366 W m^{-2}, 60°, 0.1, 9 km, and 2 km, respectively.

and shapes as a function of height and humidity captured by a replicator balloon sounding system. It is found that ice crystals present various shapes in the atmosphere and that that larger ice crystals are normally located in the lower part of cloud while smaller ones are in the upper part. Ice crystal effective size and shape have significant effect on the single-scattering properties of ice clouds and the associated cloud radiative forcing. According to equations (2.82)–(2.83), smaller D_e corresponds to larger extinction coefficient or optical depth, large single-scattering albedo, and smaller asymmetry factor, which would result in more scattering in the backward direction. Figure 2.9 shows the solar, thermal IR, and net radiative forcings for cirrus clouds as functions of IWP for various ice crystal sizes under two ice crystal shape distributions, 100% hexagonal and mixed habit, respectively, in the standard atmospheric condition. It can be seen that for a given IWP, cirrus clouds containing smaller effective sizes reflect more solar radiation and trap more thermal infrared radiation. For the same ice crystal effective size, the radiative forcings under various shapes of ice crystals would also substantially differ, as evidenced in Figure 2.9.

Theoretical and experimental studies also demonstrate the importance of ice particle roughness and irregularity in determining their radiative effect (Baran, 2012). Ulanowski et al. (2006) experimentally measured the scattering pattern of laboratory grown ice analog crystals and suggested that ice crystals with rough surfaces could reflect almost twice as much incident solar radiation than their smooth counterparts. Using a comprehensive in situ data set of ice crystal complexity coupled with measurements of the cloud angular scattering functions collected during a number of observational airborne campaigns at diverse geographical locations, Järvinen et al. (2018) demonstrated that an overwhelming fraction (~61%–81%) of atmospheric ice crystals sampled in the different regions contains mesoscopic deformations. The influence of ice particle surface roughness on the ice cloud radiative effect was estimated through simulations using the Fu-Liou radiation scheme and the GCM version of the Rapid Radiative Transfer Model (RRTMG) and the National Center for Atmospheric Research Community Atmosphere Model (Yi et al., 2013). Their results indicate that ice particle surface roughness may lead to a global-averaged shortwave cloud radiative effect of about 1–2 W m^{-2} and a small but nonnegligible increase in the global longwave cloud radiative effect. By assuming an irregular ice crystal, Zhang et al. (1999) demonstrated that small ice particles could cool the Earth's surface by ~40 W m^{-2}, and larger particles could warm the surface by ~20 W m^{-2}.

Since 1980s, development in cloud modeling has included prognostic equations for the prediction of IWC for high-level clouds formed in GCMs and climate models. This is a milestone accomplishment from the standpoint of incorporating a physically based cloud microphysics scheme in these models, and at the same time, it is also essential from the perspective of studying cloud-radiation interactions. However, cloud particle size is also an important independent parameter that affects radiation transfer. Ice crystal size and shape in the Earth's atmosphere are complex and intricate. After initial homogeneous and/or heterogeneous nucleation involving suitable aerosol particles and atmospheric conditions, ice crystal growth is governed by diffusion processes and subsequent actions by means of collision and coalescence. These physical processes are complicated by the nature of the ice crystal's hexagonal and irregular shape. Incorporating a fully interactive ice microphysics based on the first principle in a GCM appears to be a challenging but an extremely difficult computational task. Innovative D_e parameterization based on theory and observation must be developed for GCM applications.

It has been a common practice to prescribe a mean effective ice crystal size in GCMs (see, e.g., Gu et al., 2003). A number of GCMs have also used temperature to determine D_e (Gu & Liou, 2006; Kristjansson et al., 2005). This approach is rooted in earlier ice microphysics observations from aircraft, and attests to the fact that small and large ice crystals are related to cold and warm temperatures in cirrus cloud layers. Ou and Liou (1995) developed a parameterization equation relating cirrus temperature to a mean effective ice crystal size based on a large number of midlatitude cirrus microphysics data presented by Heymsfield and Platt (1984). Ou et al. (1995) reduced large standard deviations in the size-temperature parameterization by incorporating a dimensional analysis between IWC and D_e. Using CEPEX data, McFarquhar et al. (2003) developed a D_e parameterization as a function of IWC for use in a single column model.

Liou et al. (2008) have developed an ice microphysics parameterization to include interactive mean effective ice crystal size D_e in connection with radiation parameterizations. Correlation analysis between IWC and D_e has been carried out using a large set of observed ice crystal size distributions obtained from a number of cirrus field campaigns in the tropics, midlatitude, and Arctic. It is shown that IWC and D_e are well correlated using this regional division (Fig. 2.10). Including temperature classification in midlatitude cases increases this correlation. Using least-squares fitting to the observed data, the parameterization of mean effective ice crystal size in polynomials in terms of ice water content, with various coefficients for the three different regions, has been obtained. Simulations from the UCLA GCM employing this parameterization showed substantial regional deviations in outgoing longwave radiation (OLR) and precipitation patterns from assuming a prescribed constant D_e. In a more recent study, Guignard et al. (2012) also suggested that the dependence of D_e on temperature was found to be weak and that D_e is better related to IWP as this relationship was found to be more robust.

Recent development in association with cloud process modeling in climate models has been focused on the introduction of more complex representations of microphysical processes, with the dual goals of coupling them better to atmospheric aerosols and linking them more consistently to the subgrid variability assumed by the model for other calculations (IPCC, 2013). For example, more models participating in CMIP5 predict both mass and number mixing ratios for liquid stratiform cloud. Some models explicitly treat subgrid cloud water variability for calculating microphysical process rates (e.g., Morrison & Gettelman, 2008). Ice cloud treatments are similar to those for liquid water but face greater challenges because of the complexity of ice processes. Many CMIP3 models predicted the condensed water amount in just two categories—cloud and precipitation—with a temperature-dependent partitioning between liquid and ice within either category. Although supersaturation with respect to ice is commonly observed at low temperatures, only one CMIP3 GCM (ECHAM) allowed ice supersaturation (Lohmann & Kärcher, 2002).

2.5.2. Cloud Vertical Overlap

As previously mentioned, clouds have a typical length scale of perhaps several hundred meters and display substantial horizontal variability on scales that are generally smaller than the usual AGCM grid box. This introduces the cloud overlap problem for the calculation of radiative transfer under cloudy conditions, which is an important issue in climate model studies. Various parameterizations of cloud overlap effects have been developed, and several AGCM-sensitivity tests have been performed (e.g., Chou

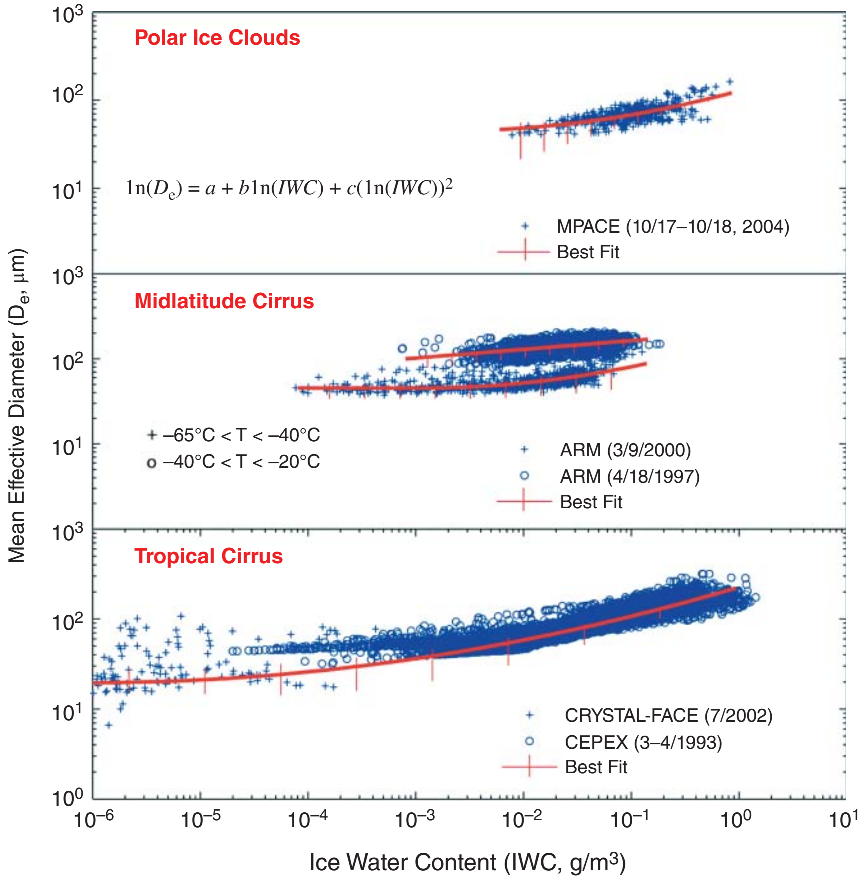

Figure 2.10 Mean correlation curves with standard deviations (vertical bars) for IWC and D_e for the tropics (bottom panel), midlatitude (middle panel), and Arctic region (top panel). Source: Liou et al. (2008)/John Wiley & Sons.

et al., 1998; Collins, 2001; Gu & Liou, 2001; Liang & Wang, 1997).

Previous commonly used approaches to treat cloud vertical overlap include random overlap, maximum overlap, and maximum/random overlap. The most straightforward approach to dealing with fractional cloud cover is the random overlap, in which the sky is divided into sectors within which the cloud amount is either 0 or 1. Radiative fluxes are calculated for each sector and then weighted by the respective cloud amount to obtain grid box fluxes. There could be a lot of possible cloud configurations (2^n possible cloud configurations, where n = total number of cloud layers). Therefore, this method could be computationally very time consuming. It also neglects cloud geometry association and tends to overestimate total cloud cover. In maximum overlap, clouds are closely associated and stack on each other. Thus, there are only two possible cloud configurations and are computationally efficient. However, this method tends to underestimate total cloud cover. In maximum/random overlap, clouds are grouped as regions, for example, by height or by adjacent and discrete clouds. Within each region, maximum overlap is assumed. For clouds of the different regions, random overlap is applied. The most common methods used in contemporary AGCMs are random overlap (Manabe & Strickler, 1964) and maximum/random overlap (Chou et al., 1998; Geleyn & Hollingsworth, 1979). The latter has been shown to be more consistent with the observed cloud distribution (Tian & Curry, 1989).

As an example, Figure 2.11 shows the possible cloud configurations if clouds are grouped as low, middle, and high regions. An atmospheric column, therefore, can be divided into at most eight sectors if clouds are present in all of the three groups. The number of configurations reduces to four if no cloud occurs or if the cloud is overcast in one of the cloud groups. If the cloud amounts in the three groups are $C1$, $C2$, and $C3$, the fractional area for the cloudy case is $C1 \times C2 \times C3$, while for the clear case it is $(1 - C1) \times (1 - C2) \times (1 - C3)$. Radiation calculations can then be performed for each of the cloud configurations, and the all-sky flux can be determined as the weighted sum of the flux computed for each sector. To implement the cloud overlap scheme in the radiation

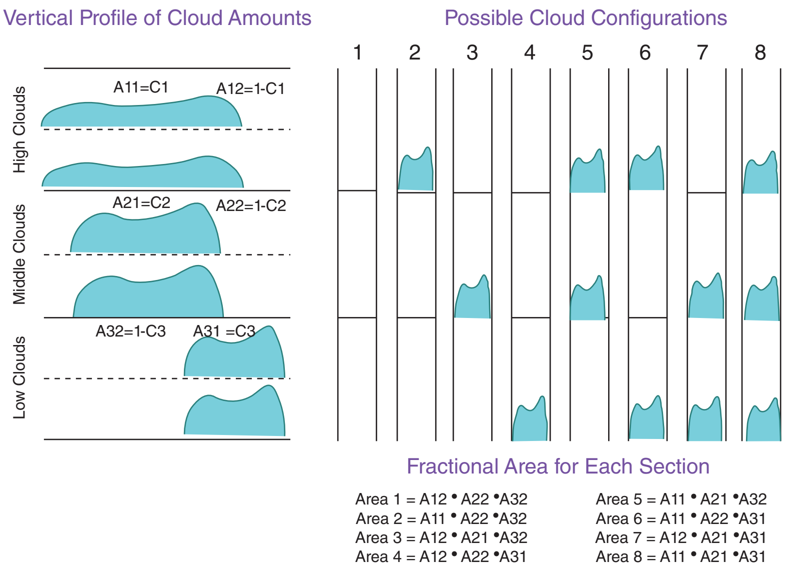

Figure 2.11 An example of possible cloud configurations.

calculation, the optical properties for clear and overcast conditions for each layer are first determined. A combination of the optical properties for clear or overcast conditions corresponding to each layer is then configured throughout the entire atmospheric column. Radiative transfer calculations can subsequently be applied to each configuration to obtain the radiation fluxes at each layer.

While in many models, the maximum/random overlap has been applied in which vertically continuous cloudy layers are assumed to overlap maximally and layers separated by noncloudy layers are assumed to overlap randomly, these assumptions have not been systematically evaluated with a comprehensive data set that can resolve simultaneously occurring cloud layers. Based on high vertical resolution cloud radar data in the United Kingdom, Hogan and Illingworth (2000) examined the overlap characteristics of clouds and found that vertically continuous clouds do not tend to be maximally overlapped, which is contrary to the assumption made in most models. A simple inverse-exponential expression for the degree of overlap as a function of level separation is then proposed, which could be implemented in current GCMs with relatively little difficulty. Using long-term cloud radar data collected by continuously operating millimeter-wavelength instruments deployed at the Atmospheric Radiation Measurement sites in the tropics, middle latitudes, and the Arctic, and the approach proposed by Hogan and Illingworth (2000), Mace and Benson-Troth (2002) also concluded that an assumption of random overlap for layers separated by noncloudy layers is supported by observations. However, the overlap characteristics of vertically continuous layers cannot be considered maximal. Indeed, vertically continuous cloudy layers do not appear to be able to represented by a simple overlap assumption. They also showed that the cloud-layer overlap characteristics in the middle latitudes appear to be a strong function of season, suggesting that an overlap parameterization in terms of cloud system type may be possible.

2.5.3. Cloud Inhomogeneity Effects

Satellite mapping of the optical depth in midlatitude and tropical regions has illustrated that cirrus clouds are frequently finite in nature and display substantial horizontal variabilities (Minnis et al., 1993; Ou et al., 1995). Vertical inhomogeneity of the ice crystal size distribution and ice water content has also been demonstrated in the microphysics balloon sounding observations (Heymsfield and Miloshevich, 1993). Figure 2.12 shows a 3D cirrus from Lidar observations. The data were obtained by the scanning of Lidar across the moving direction of the clouds. The observed cirrus clouds over an area of 24×24 km at altitudes from 6 to 12 km were shown to be highly inhomogeneous. Based on 3D radiative transfer calculations, cloud inhomogeneity has been shown to play a significant role in the heating rate profile averaged over mesoscale grids, and the result differs from that computed from the conventional plane-parallel approach (Gu & Liou, 2001). However, creating representations of cloud inhomogeneity in general circulation models for climate study is a difficult task since they generally have spatial scales greater than 100 km primarily due to computational limitations. Moreover, the relationship between the cloud optical properties (in terms of optical depth) and radiative fluxes is nonlinear, leading to